Journal of Vibration Engineering & Technologies (2026) 14:87
https://doi.org/10.1007/s42417-025-02301-x

ORIGINAL PAPER

A Crack Location Index for Crack Detection in Beam-Like Structures Carrying a Roving Mass

X. Sun[1] · S. Ilanko[1] · Y. Mochida[1] · R. C. Tighe[1] · B. R. Mace[2]

Received: 26 August 2025 / Revised: 14 December 2025 / Accepted: 18 December 2025

Abstract

Purpose Vibration-based damage identification methods rely on robust damage indices to detect and localize structural defects. While natural frequency shifts are often cost-effective and easily obtainable, their sensitivity to minor damage and dependence on baseline (intact) data remain key challenges. Existing roving-mass-based methods often suffer from mass-induced modal fluctuations that generate false peaks in frequency-location curves, limiting their reliability for crack localization. This study aims to develop a robust crack location index for beam-like structures that improves crack localization accuracy when a roving mass with rotary inertia traverses a crack, while relying primarily on measured natural frequencies.

Methods An analytical expression for natural frequency estimation is derived and validated against results from the Dynamic Stiffness Method, forming the basis for the index formulation. The proposed index integrates measured natural frequencies with analytically available modal properties of an intact Euler-Bernoulli beam, allowing false peaks to be suppressed without requiring baseline frequency measurements.

Results Numerical studies demonstrate that the index reliably identifies single and multiple cracks and performs consistently across different boundary conditions, with the combined use of the 2nd and 3rd modes providing the most stable diagnostic signatures. Experimental validation confirms the index's superiority over the change of natural frequency shift; the results show that the index can pinpoint crack locations with high accuracy without requiring experimental baseline measurements from the undamaged structure.

Conclusion The proposed index provides a robust and baseline-free approach for crack localization in beam-like structures. By incorporating intact-beam modal information into post-processing, the method improves damage identifiability.

Keywords Roving mass · Rotary inertia · Crack detection · Beam · Dynamic stiffness method

Introduction

Structural Health Monitoring (SHM) relies on the development and application of reliable and robust indices capable of identifying, quantifying, and, when feasible, predicting damage in structures to avoid severe consequences [1]. Vibration-based damage identification is a promising approach in SHM based on the dynamic response characteristics of structures. When damage occurs, modal parameters such as natural frequencies, mode shapes, and modal damping are altered due to damage-induced changes in physical properties such as the mass, damping, and, in particular, stiffness of the structure. The variation of modal parameters due to damage enables the formulation of a structural inverse problem, in which the objective is to reconstruct local changes in physical properties, thus revealing the presence, location, and severity of any damage. Vibration-based damage identification has gained considerable attention in research due to several advantages. Firstly, such methods are generally cost-effective and do not require extensive instrumentation. For example, it is possible to extract the dynamic characteristics of large or complex structures using a limited number of sensors. Secondly, most vibration-based techniques require equipment that is compact, user-friendly, and convenient to mount on the target structure. Thirdly, vibration-based methods do not require prior knowledge of

✉ Y. Mochida
yusuke.mochida@waikato.ac.nz

[1] The School of Engineering, University of Waikato, Hamilton 3216, New Zealand

[2] Department of Mechanical and Mechatronics Engineering, University of Auckland, Auckland 1010, New Zealand

Published online: 29 January 2026

the possible damage location, which makes them suitable for global monitoring.

Damage Indices

A widely adopted strategy for solving the structural inverse problem involves developing indices that are highly sensitive to structural damage. These indices are often based on different modal characteristics such as natural frequency, mode shape, modal curvature, modal strain energy, and modal flexibility [2]. For example, Khanahmadi et al. [3] extended 1D mode shape signals to 2D and proposed two damage indices based on wavelet transform and signal curvature analysis. Damage locations were indicated by the discontinuities or peaks in the graph of damage indices. Zhu and Zhang [4] presented a damage index based on the frequency decay induced by breathing cracks in a concrete beam. Nick et al. [5] developed damage indices based on modal flexibility and modal strain energy and the peaks in the curves of indices showed the damage location. Brethee et al. [6] introduced damage indices based on the damage-induced changes in modal curvature of laminated composite plates. The locations of fibre breakage and delamination were indicated by the peaks in the curves of the indices. He et al. [7] took the modal curvature difference before and after the damage occurred as the damage index to identify damages in a composite cantilever beam. To tackle noise and measurement inaccuracies in modal curvature, Namah and Brethee [8] proposed another damage index based on the normalized modal curvature of individual modes to detect single and double cracks of 30% or 40% severity in beams. The index was tested on Euler-Bernoulli beams with standard boundary conditions, for which the intact modal characteristics can be computed analytically. This eliminates the need for experimental modal testing of the undamaged beams when constructing the index. In recent years, Machine Learning and Deep Learning are becoming increasingly popular and have been utilized to enhance the performance of various damage indices [9–11]. Other recent studies have also focused on developing damage indices using wavelet transforms. For example, to identify damage in columns under axial loads, Khanahmadi et al. [12] simulated the damage as a decrease of the modulus of elasticity and proposed a damage location index (DLI) based on the details of the wavelet coefficients obtained from the wavelet analysis of the mode shapes of the damaged column. The DLI was demonstrated to be largely independent of the magnitude of the axial load, which indicates the DLI's potential even near high-load conditions. Further extending these concepts to plate-like structures, Khanahmadi et al. [13] developed an irregularity detection index (IDI) for 3D sandwich panels based on a validated finite element model (with the damage defined as a reduction of the modulus of elasticity of the concrete layer). Their approach utilizes 2D wavelet analysis of combined primary and secondary mode shapes to identify damaged regions. The IDI shows monotonic sensitivity to damage severity, which potentially allows qualitative severity assessment apart from localization. It was also found that damage detection at one location does not interfere with detection at other locations, which suggests low 'cross-talk' in IDI and clearer interpretation. To address the specific challenge of interface debonding, Khanahmadi et al. [14] developed a mode shape sensitivity-based wavelet feature extraction method for concrete-filled steel tubes. Debonding was simulated as a uniform reduction of the concrete modulus of elasticity at the interface to at least 3 mm depth. They proposed a total normalized irregularity detection index integrating horizontal, vertical, and diagonal detail coefficients from 2D discrete wavelet transform applied to corrected modal signals. Debonding near column ends, a region typically problematic due to boundary stiffness and mode shape curvature, was also investigated. In another study, instead of assessing the accumulation of irregularities, Khanahmadi et al. [15] focused on the direct identification of irregularity peaks in an irregularity detection index at the sites of debonding based on modal signal processing using 2D wavelet transform. As the severity of debonding increases, the corresponding irregularity peak identified by the index also increases.

Among different damage indices, natural frequency shift is the most straightforward and intuitive index for signalling the presence of damage. Methods using natural frequencies have been extensively investigated as frequency measurements are often efficient and reliable. However, such methods also face limitations. One key challenge lies in the measurability of damage-induced natural frequency changes, particularly when the damage is minor or when the measurements are affected by considerable noise. From this perspective, Sun et al. [16] investigated the feasibility of natural frequency-based crack detection combining frequency shift measurability and structural integrity, which indicates that the material's ductility or brittleness can influence the measurability substantially.

The Roving Mass Technique

Apart from the detectability of a frequency shift, the absence of baseline information (i.e. the natural frequencies of the intact structure) poses another challenge – identifying damage location solely from the altered natural frequencies that do not contain any spatial information of the damage. To address this, several researchers have introduced an auxiliary mass as a probe to assist damage identification. For example, by sequentially attaching a mass at different points

along a beam - an approach commonly referred to as the stationary roving mass technique - a curve of natural frequency versus mass location can be obtained. Applying a wavelet transform to the curve allows for the exposure of crack-induced local perturbations in the detail coefficients, which can effectively reveal the crack location [17, 18]. The roving mass technique has also been extended to other structures such as rectangular plates [19] and cylindrical shells [20] where local thickness reductions were introduced as damage and the accelerometer served as the auxiliary mass. In [19], by positioning the accelerometer at various points on the plate and measuring the fundamental natural frequency, a frequency shift surface was established. Local changes in the curvature of this surface revealed the damage location. In [20], the accelerometer roved around the cylindrical shell's circumference and a frequency shift curve (similar to the curve of frequency versus mass location in beams) was obtained, with the lowest point on the curve indicating damage location.

The natural frequency shift caused by a roving mass passing over a crack has been confirmed with high-precision frequency measurement systems such as quasi-optical coherence vibration tomography in [21], however, the depth of the introduced saw cut reached half of the thickness of the tested beam, indicating a relatively severe crack. Wang et al. [22] constructed a spatial curve named the frequency shift path by roving an accelerometer (serving as an auxiliary mass) along a beam. The main characteristic of the spatial curve is that its projection onto the time-frequency plane is the conventional curve of natural frequency versus mass location, and its projection onto the time-amplitude plane approximates the power mode shape [23]. Thus the spatial curve contains information of both frequency shift and amplitude variation induced by the mass traversing a damaged region. The curvature of the spatial curve was taken as the damage index, and damage corresponding to 25% or 50% of beam thickness reduction was located. To improve the accuracy of crack detection, Solís et al. [24] introduced a methodology that integrates the roving mass technique with baseline data. As the mass was sequentially repositioned along the beam, experimental modal analysis was conducted at each position. The difference between the damaged and undamaged mode shapes was then analysed using wavelet transform. To enhance damage sensitivity, wavelet coefficients across all mass positions were summed based on weighting parameters derived from the natural frequency shifts between damaged and intact states, as well as the estimated noise levels for each mode. This weighting emphasized contributions from mode shapes that were both strongly affected by damage and exhibited low noise. In experimental validation, damage levels corresponding to 10%, 20%, and 50% thickness reductions were detected. However, the identification of the 10% damage case proved less reliable due to increased sensor-induced noise, which tended to obscure the damage signature.

Beyond its application to common beams and plates, the stationary roving mass technique has also been employed for crack detection in other structural models such as a compressed natural gas cylinder [25], a railway track model [26], a layered beam model [18], a double-beam system [27], and a roving disc [28]. In the aforementioned studies, the influence of the roving mass was typically limited to its translational inertia during vibration, while the effect of rotary inertia was neglected. To address this limitation, Cannizzaro et al. [29] introduced the concept of a roving body with rotary inertia and theoretically demonstrated that when the body passes over a crack on a beam, the natural frequencies of the beam shift abruptly. The underlying rationale is that the crack brings about a rotation discontinuity of the beam cross-section, which leads to a discontinuity in the inertial moment caused by roving mass, thus noticeable frequency changes can be observed when the mass passes the discontinuity, i.e. the cracked cross-section. Since the inertial moment is proportional to frequency squared, the frequency change becomes more discernible as the mode number increases [30]. Subsequently, Ilanko et al. [31] presented a numerical study based on the Rayleigh-Ritz method where natural frequencies were calculated when a roving body with rotary inertia traverses a partial crack on a plate, and similar abrupt frequency shifts were also observed. Utilizing the frequency shifts in [29, 31], it is possible to identify damage solely from the measured natural frequencies without baseline information or prior knowledge of the structure. However, the practical measurability of such frequency shifts with respect to crack severity should be investigated. In particular, the fact that the rotary inertia, instead of acting at a point as it does in theoretical derivations, is distributed over a small contact area would potentially make the frequency shift less discernible in practice.

Recent Work

To address the above concerns, a recent paper presented theoretical and experimental investigations to verify the presence and detectability of the natural frequency shift when a roving body with rotary inertia passes over a crack [32]. A systematic comparison between experimental, theoretical, and simulation results was made in [32], which shed light on the feasibility of measuring theoretically significant frequency shift using impact hammer tests. Two cracked beams, with crack depths of 20% and 40% of the beam thickness, respectively, were tested. The natural frequency f when the mass was located at various positions along the beam was measured, from which the frequency shift

between adjacent mass locations (i.e. Δf) and the change in the frequency shift between adjacent mass locations (i.e. $\Delta(\Delta f)$) were calculated. The results demonstrated that a pronounced frequency shift can be reliably captured as the roving mass traverses the 40% crack. Although the frequency shift associated with the 20% crack was also measurable, identifying the crack location based solely on the peaks in Δf or $\Delta(\Delta f)$ curves proved insufficient for accurate crack localization. To pinpoint the crack location, a more robust crack location index than Δf and $\Delta(\Delta f)$ is needed.

While roving mass techniques are well-established, they can suffer from false alarms in damage indices caused by mass-induced modal fluctuations, as seen in [32]. Furthermore, the influence of the mass's rotary inertia is often neglected. This study aims to address this gap by developing an effective crack location index that specifically accounts for rotary inertia and integrates measured frequency shifts with analytical modal information of the intact beam to attenuate mass-induced false alarms and isolate the true crack-induced signature. The method is considered 'baseline-free' as it does not require frequency measurements from the intact state of the damaged structure. Instead, it utilizes the theoretical modal properties of a generic intact beam, which are readily available [33].

The remainder of the paper is structured as follows. In Sect. 2, an analytical expression for estimating the natural frequency of an Euler-Bernoulli beam carrying a roving mass with rotary inertia is derived and verified against results obtained from the Dynamic Stiffness Method (DSM) [30, 34, 35]. Based on this formulation, the crack location index is developed. Section 3 evaluates the robustness of the crack location index through numerical studies based on the DSM model, incorporating different crack locations, various boundary conditions, and multi-crack identification. Section 4 provides an overview of the experimental set-up, introduces the process of natural frequency extraction from the measured signal, and discusses results for the 20% cracked beam. The applicability of the proposed index is experimentally verified using the 20% and 40% cracked beams. Finally, Sect. 5 concludes the study by summarizing the main findings, discussing limitations, and outlining directions for future work.

Crack Location Index

This section describes the development of a crack location index. An analytical expression for estimating the natural frequency of an Euler–Bernoulli beam carrying a mass with rotary inertia is derived and verified against results obtained from the DSM. Based on this formulation, the crack location index is defined.

The Equation for Natural Frequency Estimation

Figure 1 shows a uniform Euler-Bernoulli beam carrying a roving mass with rotary inertia where M and J denote the translational inertia and rotary inertia of the roving mass, respectively, and x_0 is the coordinate of the mass location. The mathematical model developed in this paper is based on Euler-Bernoulli beam theory. This assumption is justified by the high slenderness ratio of the beam investigated in this work (as detailed in Sect. 3). For such a slender beam, the effects of shear deformation and the rotary inertia of the beam cross-section are negligible for the lower vibration modes considered [36, 37]. It should be noted, however, that while the beam's rotary inertia is neglected, the rotary inertia of the roving mass, J, is explicitly included in the formulation, as it is a localized effect that significantly influences the frequency shifts as the mass traverses the crack.

Consider the free-body diagram of an element of the beam of length dx as shown in Fig. 2, where $M_b(x,t)$ is the bending moment, $F(x,t)$ is the shear force, and $v(x,t)$ is the transverse deflection of the beam. The force equilibrium gives

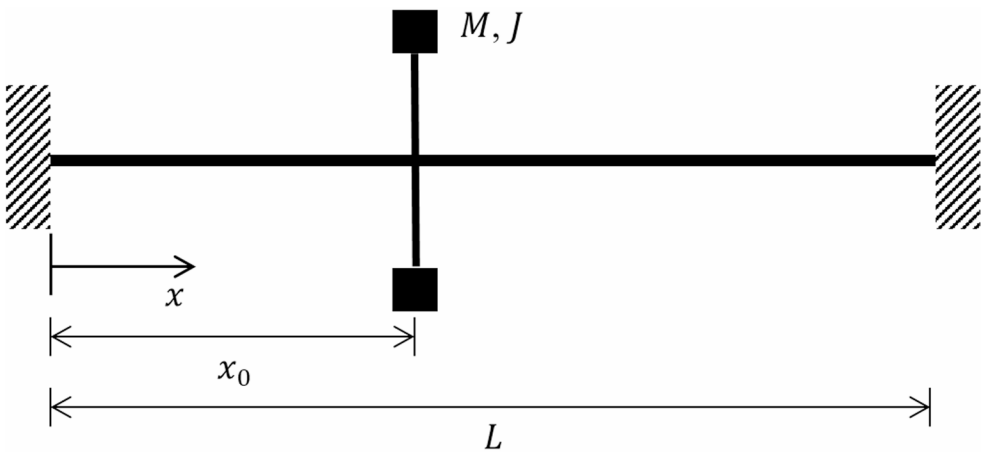

Fig. 1 A beam carrying a roving mass with rotary inertia

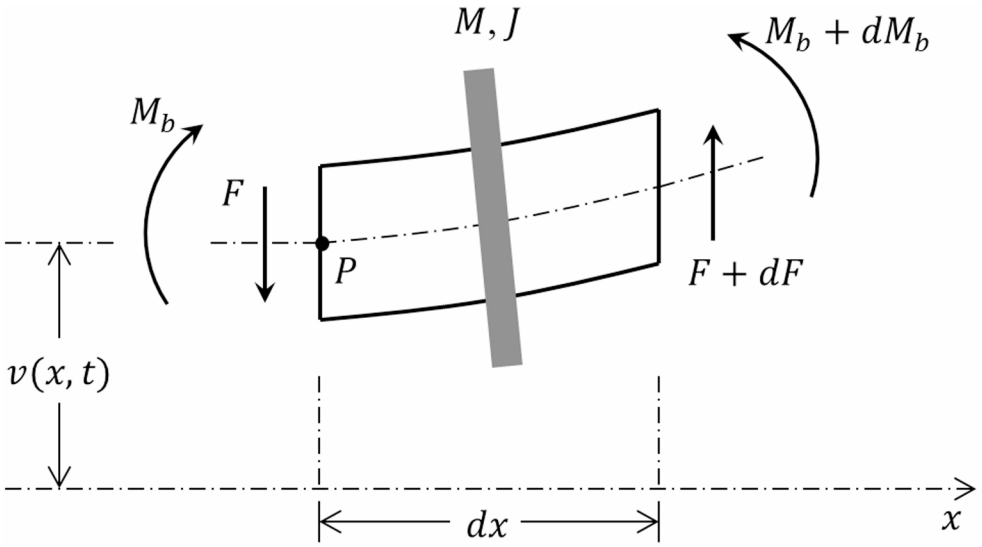

Fig. 2 The free-body diagram of a beam element in transverse vibration

$$-F+(F+dF)=\bar{m}\ddot{v}dx+M\ddot{q}_M(t)\,\delta\,(x-x_0)\,dx \tag{1}$$

where $\bar{m}$ is mass per unit length, $q_M(t)$ is the transverse displacement of the mass, $\delta\,(x-x_0)$ is the Dirac delta function, and the overdot represents the derivative with respect to time. The moment equilibrium equation about point P leads to

$$-M_b+(M_b+dM_b)+(F+dF)\,dx=J\ddot{\theta}\,(t)\,\delta\,(x-x_0)\,dx \tag{2}$$

where $\theta\,(t)$ is the rotation of the mass. Writing $dF=\frac{\partial F}{\partial x}dx$ and $dM_b=\frac{\partial M_b}{\partial x}dx$ and disregarding terms involving second powers of dx, Eqs. (1) and (2) can be written as

$$\frac{\partial F}{\partial x}=\bar{m}\ddot{v}+M\ddot{q}_M(t)\,\delta\,(x-x_0) \tag{3}$$

$$F=-\frac{\partial M_b}{\partial x}+J\ddot{\theta}\,(t)\,\delta\,(x-x_0) \tag{4}$$

Substituting Eq. (4) into Eq. (3) gives

$$-\frac{\partial^2 M_b}{\partial x^2}+J\ddot{\theta}\,(t)\,\delta'\,(x-x_0)=\bar{m}\ddot{v}+M\ddot{q}_M(t)\,\delta\,(x-x_0) \tag{5}$$

where the prime represents the derivative with respect to x. For a uniform Euler-Bernoulli beam, the relationship between bending moment and deflection can be expressed as [37]

$$M_b(x,t)=EI\frac{\partial^2 v(x,t)}{\partial x^2} \tag{6}$$

where EI is flexural rigidity. Inserting Eq. (6) into Eq. (5), the governing equation of motion of the beam becomes:

$$\bar{m}\ddot{v}(x,t)+EIv''''(x,t)=J\ddot{\theta}\,(t)\,\delta'\,(x-x_0)-M\ddot{q}_M(t)\,\delta\,(x-x_0) \tag{7}$$

The mass is rigidly attached to the beam, thus

$$q_M(t)=v(x_0,t) \tag{8}$$

$$\theta\,(t)=v'\,(x_0,t) \tag{9}$$

Using the modal superposition method [38–40], the beam deflection can be expressed as

$$v(x,t)=\sum_n \phi_n(x)\,q_n(t) \tag{10}$$

where $\phi_n(x)$ is the nth mode shape of the beam without the attached mass, found by solving the equation [41]

$$EI\phi_n''''(x)-\bar{m}\omega_{bn}^2\phi_n(x)=0 \tag{11}$$

and $q_n(t)$ is the generalized coordinate or modal participation coefficient. In Eq. (11), ω_{bn} is the nth natural frequency of the bare beam (i.e. the beam without the mass).

Substituting Eqs. (8)-(10) into Eq. (7) and multiplying by $\phi_m(x)$ on both sides and integrating over the whole beam yields

$$\begin{aligned}&\int_0^L \bar{m}\phi_m(x)\sum_n \phi_n(x)\ddot{q}_n(t)\,dx+\int_0^L EI\phi_m(x)\sum_n \phi_n''''(x)\,q_n(t)\,dx=\\&\int_0^L \phi_m(x)\left[J\sum_n \phi_n'(x_0)\ddot{q}_n(t)\right]\delta'\,(x-x_0)\,dx-\\&\int_0^L \phi_m(x)\left[M\sum_n \phi_n(x_0)\ddot{q}_n(t)\right]\delta\,(x-x_0)\,dx\end{aligned} \tag{12}$$

Considering the orthogonal property of mode shapes [37]

$$\int_0^L \phi_m(x)\,\phi_n(x)\,dx=\begin{cases}0 & (m\neq n)\\ \psi_m & (m=n)\end{cases} \tag{13}$$

the first term on the left-hand side of Eq. (12) can be simplified as

$$\int_0^L \bar{m}\phi_m(x)\sum {}_n\phi_n(x)\,\ddot{q}_n(t)\,dx = \bar{m}\psi_m\ddot{q}_m(t) \tag{14}$$

Considering Eq. (11) and Eq. (13), the second term on the left-hand side of Eq. (12) can be written as

$$\int_0^L EI\phi_m(x)\sum {}_n\phi_n''''(x)\,q_n(t)\,dx = \bar{m}\omega_{bm}^2\psi_m q_m(t) \tag{15}$$

Using Eq. (13) and the sifting property of δ function, the right-hand side of Eq. (12) can be expressed as

$$\begin{aligned}&\int_0^L \phi_m(x)\left[J\textstyle\sum_n \phi'_n(x_o)\,\ddot{q}_n(t)\right]\delta'(x-x_o)\,dx-\\ &\int_0^L \phi_m(x)\left[M\textstyle\sum_n \phi_n(x_o)\,\ddot{q}_n(t)\right]\delta(x-x_o)\,dx=\\ &-J\phi'^2_m(x_o)\,\ddot{q}_m(t)-M\phi^2_m(x_o)\,\ddot{q}_m(t)-R_1-R_2\end{aligned} \tag{16}$$

where

$$R_1 = J\phi'_m(x_0)\sum {}_{i\neq m}\phi'_i(x_0)\,\ddot{q}_i(t) \tag{17}$$

$$R_2 = M\phi_m(x_0)\sum {}_{i\neq m}\phi_i(x_0)\,\ddot{q}_i(t) \tag{18}$$

Therefore, rearranging and rewriting Eq. (12) gives

$$\begin{aligned}&\left[\bar{m}\,\psi_m + M\phi_m^2(x_0) + J\phi_m'^2(x_0)\right]\ddot{q}_m(t)+\\ &\bar{m}\,\omega_{bm}^2\psi_m q_m(t) = -R_1-R_2\end{aligned} \tag{19}$$

By neglecting the cross-modal terms i.e. R_1 and R_2 on the right-hand side of Eq. (19), the mth natural frequency of the beam carrying a mass at x_0 can be approximated as

$$\omega_m^2(x_0) = \frac{\omega_{bm}^2}{1+\frac{M\phi_m^2(x_0)+J\phi_m'^2(x_0)}{\bar{m}\psi_m}} \tag{20}$$

From Eq. (20), ω_m is dependent on the natural frequency of the bare beam and the modal data of the bare beam at the mass location. It can be seen how M and J come into play. The presence of M and J reduces ω_m. M is involved by multiplying the mode shape squared at the mass location, while the dependence of J involves the modal slope at the mass location. This explains the fluctuation of the curve of natural frequency versus mass location in Sect. 4.3. Equation (20) also reflects why natural frequency shifts occur when a roving mass with rotary inertia passes over a crack. A crack brings about a discontinuity in $\phi'_m(x)$, which leads to a discontinuity in ω_m through the term $J\phi'^2_m$. Therefore, incorporating rotary inertia amplifies the frequency shift when the mass passes the crack.

The expression for the change in natural frequency can be found by taking the first derivative of ω_m with respect to mass location, i.e.

$$\frac{d\omega_m(x)}{dx} = \frac{-\omega_{bm}\sqrt{\bar{m}\psi_m}\left[M\phi_m(x)\phi'_m(x)+J\phi'_m(x)\phi''_m(x)\right]}{\left[\bar{m}\psi_m+M\phi_m^2(x)+J\phi'^2_m(x)\right]^{\frac{3}{2}}} \tag{21}$$

From Eq. (21), apart from the mode shape and modal slope, $\frac{d\omega_m(x)}{dx}$ is also related to $\phi''_m(x)$, i.e. the modal curvature of the bare beam at the mass location. As $\phi_m(x)$, $\phi'_m(x)$, and $\phi''_m(x)$ are not independent of each other, it is impossible to deduce the extrema of ω_m and $\frac{d\omega_m(x)}{dx}$ directly from the extrema of $\phi_m(x)$, $\phi'_m(x)$, or $\phi''_m(x)$. However, the involvement of modal data in the expressions of ω_m and $\frac{d\omega_m(x)}{dx}$ provides some insights for devising the crack location index in Sect. 2.3.

Numerical Verification

While an exact expression for the natural frequency of a beam carrying a mass is not available, to verify the accuracy of Eq. (20), the natural frequency of a simply supported steel beam carrying a mass with rotary inertia is calculated using the DSM. The dimensions of the beam and the mass location are shown in Fig. 3. For the material properties, the density ρ is 7850 kg/m^3, the elastic modulus E is 200GPa, and the Poisson's ratio ν is 0.3.

The rotary inertia of the beam J_{beam} is calculated about the central axis O' as shown in Fig. 3. τ and φ are dimensionless parameters defined as the ratios between the mass

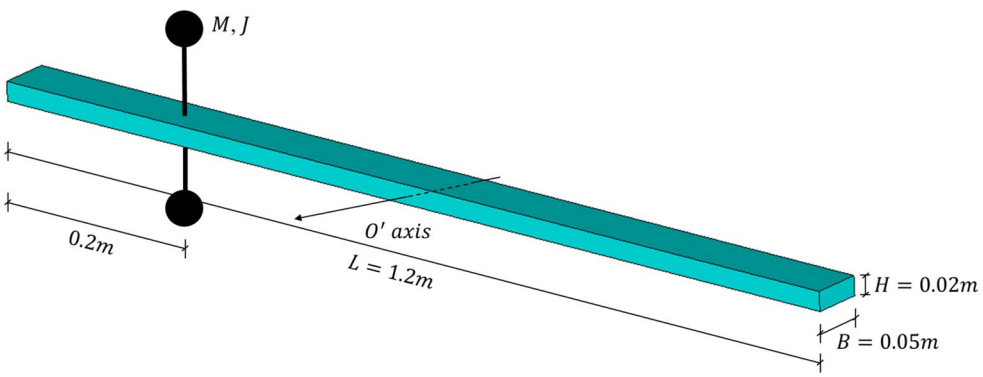

Fig. 3 The geometry of the simply supported beam carrying a mass with rotary inertia

and beam for quantifying the translational inertia and rotary inertia of the mass, and are expressed as

$$\tau = \frac{M}{M_{beam}} \tag{22}$$

$$\varphi = \frac{J}{J_{beam}} \tag{23}$$

For a simply supported beam without a mass, the formulas for the natural frequencies and mode shapes can be found in [33]. When $\tau = 0.1$ and $\varphi = 0.001$, the natural frequencies are listed in Table 1.

Table 1 shows that Eq. (20) gives a very good estimate of the natural frequency of a beam carrying a mass with rotary inertia. For the same beam carrying the same mass but with various boundary conditions (such as clamped-clamped, clamped-pinned, clamped-free, sliding-pinned, etc.), a comparison of the results against the DSM results is listed in the Appendix A. Overall, Eq. (20) demonstrates satisfactory accuracy in natural frequency estimation.

Crack Location Index

By sequentially attaching a mass with rotary inertia to different positions along a beam, natural frequencies can be measured with respect to the mass location. The resulting frequency shifts occurring as the mass traverses a crack can be used to identify the crack location. Here it should be noted how the natural frequency shift (i.e. Δf) and the change of natural frequency shift (i.e. $\Delta(\Delta f)$) are calculated. When f_i represents the natural frequency evaluated when the mass is at the ith position (i=1, 2, 3, …), the natural frequency shift after the mass is moved from the $(i-1)$ th to the ith position can be expressed as

$$\Delta f_i = f_i - f_{i-1} \quad (i = 2,\ 3,\ 4, \dots) \tag{24}$$

Table 1 Natural frequencies obtained through the DSM and Eq. (20)

Mode number	DSM results (rad/s)	Equation (20) results (rad/s)	Percentage error (%)
1	194.75	194.92	0.09
2	744.64	745.00	0.05
3	1661.60	1641.00	1.24
4	3031.07	2979.74	1.69
5	4843.61	4870.20	0.55
6	6957.92	7182.00	3.22
7	9281.31	9540.22	2.79
8	12049.70	11914.86	1.12
9	15263.28	14769.00	3.24
10	18076.71	18612.19	2.96

Repeating this procedure for the natural frequencies evaluated at all mass locations, the resulting curves of Δf are obtained. The change of natural frequency shift (i.e. $\Delta(\Delta f)$) is also calculated as an attempt to highlight the crack location. $\Delta(\Delta f)$ is defined as follows

$$\Delta\ (\Delta f_i) = \Delta f_i - \Delta f_{i-1} \quad (i = 3,\ 4,\ 5, \dots) \tag{25}$$

Therefore, $\Delta(\Delta f)$ is the difference between the Δf when the mass is located in two adjacent positions.

It is shown in [32] that false peaks in the curve of $\Delta(\Delta f)$ versus mass location make it challenging to determine the crack location. To suppress those peaks in $\Delta(\Delta f)$, a crack location index ζ is introduced. When the coordinate of the mass location is x_0, the crack location index for the mth mode at x_0, i.e. $\zeta_m(x_0)$, is defined as

$$\zeta_m(x_0) = \Delta\ (\Delta f_m)|_{x_0} \bullet \phi'_m(x_0) \bullet \phi'''_m(x_0) \tag{26}$$

For an intact beam carrying a mass at x_0, it is shown in Eq. (20) that ω_m (or f_m) is directly related to $\phi_m(x_0)$ and $\phi'_m(x_0)$. It is also shown in Eq. (21) that $\frac{d\omega_m(x)}{dx}$ (or Δf_m) depends on $\phi_m(x)$, $\phi'_m(x)$, and $\phi''_m(x)$. This observation motivates the formulation of the crack location index ζ which employs the zero points of $\phi'_m(x)$ and $\phi'''_m(x)$ to attenuate the extrema of $\Delta(\Delta f)$, thereby suppressing false peaks and isolating the peak corresponding to the crack location. The rationale behind the formulation of ζ is demonstrated as follows.

Equation (21) can be rewritten as

$$\frac{d\omega_m(x)}{dx} = -K_m Q_m(x)\, G_m^{-\frac{3}{2}}(x) \tag{27}$$

where

$$K_m = \omega_{bm}\sqrt{\bar{m}\psi_m} \tag{28}$$

$$Q_m(x) = M\phi_m(x)\,\phi'_m(x) + J\phi'_m(x)\,\phi''_m(x) \tag{29}$$

$$G_m(x) = \bar{m}\,\psi_m + M\phi^2_m(x) + J\phi'^2_m(x) \tag{30}$$

Thus the 2nd and 3rd derivatives of $\omega_m(x)$ can be written as

$$\frac{d^2\omega_m(x)}{dx^2} = K_m\left[-Q'_m(x)\,G_m^{-\frac{3}{2}}(x) + \frac{3}{2}Q_m(x)\,G_m^{-\frac{5}{2}}(x)\,G'_m(x)\right] \tag{31}$$

and

$$\frac{d^3\omega_m(x)}{dx^3} = K_m\frac{-Q'''_m(x)G^2_m(x)+3Q'_m(x)G_m(x)G'_m(x)-\frac{15}{4}Q_m(x)G'^2_m(x)+\frac{3}{2}Q_m(x)G_m(x)G''_m(x)}{G_m^{7/2}(x)} \tag{32}$$

where

$$Q'_m(x) = M\left[\phi'^{\,2}_m(x) + \phi_m(x)\,\phi''_m(x)\right] + J\left[\phi''^{\,2}_m(x) + \phi'_m(x)\,\phi'''_m(x)\right] \tag{33}$$

$$Q''_m(x) = M\left[3\phi'_m(x)\,\phi''_m(x) + \phi_m(x)\,\phi'''_m(x)\right] + J\left[3\phi''_m(x)\,\phi'''_m(x) + \phi'_m(x)\,\phi''''_m(x)\right] \tag{34}$$

$$G'_m(x) = 2\left[M\phi_m(x)\,\phi'_m(x) + J\phi'_m(x)\,\phi''_m(x)\right] \tag{35}$$

$$G''_m(x) = 2M\left[\phi'^{\,2}_m(x) + \phi_m(x)\,\phi''_m(x)\right] + 2J\left[\phi''^{\,2}_m(x) + \phi'_m(x)\,\phi'''_m(x)\right] \tag{36}$$

Suppose that at a given mass location x_0, $\phi'_m(x_0) = \phi'''_m(x_0) = 0$, which is possible when the mode shape $\phi_m(x)$ can be expressed using trigonometric functions (e.g. beams with pinned-pinned, sliding-pinned, and sliding-sliding boundary conditions [33]). It leads to $Q_m(x_0) = Q''_m(x_0) = G'_m(x_0) = 0$, and hence the numerator of Eq. (32) becomes zero and $\frac{d^3\omega_m(x)}{dx^3}\Big|_{x_0} = 0$, which means $\frac{d^2\omega_m(x)}{dx^2}$ reaches a local extreme at x_0. As the extrema of $\frac{d^2\omega_m(x)}{dx^2}$ are equivalent to the peaks in $\Delta(\Delta f_m)$, multiplying $\Delta(\Delta f_m)|_{x_0}$ by $\phi'_m(x_0)$ and $\phi'''_m(x_0)$ suppresses the peak when the mass coordinate is x_0. Thus Eq. (26) can be formulated.

Although the formulation of ζ can be analytically justified for beams whose mode shapes $\phi_m(x)$ can be expressed in trigonometric functions, its effectiveness may extend beyond these specific cases. This is shown in Sect. 3 with beams whose mode shapes are represented by combinations of trigonometric and hyperbolic functions (e.g. beams with clamped-clamped, clamped-pinned, and clamped-free boundary conditions [33]).

Numerical Results

To verify the effectiveness of the proposed crack location index, a series of numerical examples based on the DSM are presented in this section. The crack locations or beam boundary conditions are varied across the examples to evaluate whether the crack location index performs well under different circumstances.

Clamped-Clamped Cracked Beam

A clamped-clamped steel beam with a 20% thickness reduction crack and carrying a roving mass with rotary inertia is modelled using the DSM. The beam has dimensions of 0.623 m × 0.020 m × 0.002 m (length × width × thickness). The crack is located at 0.394 m from the left end of the beam. The spacing between adjacent mass locations is 0.004 m. The material properties of the beam and the size of the mass are listed in Table 2.

The curves of f, $\Delta(\Delta f)$, and ζ versus mass location are shown in Fig. 4(b). The modal data of the 8th mode of the clamped-clamped intact bare beam is shown in Fig. 4(a) for comparison. It can be observed that some of the local maximums of the curve of f align with the extrema of the mode shape and modal curvature of the intact bare beam. The extrema of the curve of f correspond to the peaks in the curve of $\Delta(\Delta f)$. Therefore, multiplying $\Delta(\Delta f)$ by the derivative of mode shape (i.e. $\phi'_m(x)$) and the derivative of modal curvature (i.e. $\phi'''_m(x)$) would help suppress the peaks in the curve of $\Delta(\Delta f)$. As shown in the curve of ζ, there are fewer peaks compared with the curve of $\Delta(\Delta f)$.

Although some peaks are suppressed, the remaining peaks in the curve of ζ for the 8th mode still impede the determination of crack location. However, as the mode number decreases, the number of remaining peaks in the curve of ζ reduces. The results of the 7th mode to the 1 st mode are shown in Figs. 5, 6, 7, 8, 9, 10 and 11. Observing these figures, the crack location (at 0.394 m) becomes increasingly visible in the curve of ζ as the mode number decreases. The crack location can be clearly seen in the curves of ζ for the first three modes because there are no false peaks except near the boundaries. The curve of f reaches extrema when the mass is located near the boundaries possibly due to the large contribution of $\phi'_m(x)$, and the resulting peaks in the curve of $\Delta(\Delta f)$ cannot be suppressed using the current crack location index. Therefore, the crack location index is most effective for the first three modes excluding regions near boundaries. Considering that $\Delta(\Delta f)$ for the 1 st mode does not give meaningful results in the experiment due to the small magnitude of the peak at the crack location, the 2nd and 3rd modes are used for locating the crack. It should be noted that the selection of the 2nd and 3rd modes represents an optimal balance for the application of ζ. Lower modes (e.g. mode 1) possess low modal curvature, resulting in reduced sensitivity to small cracks. Conversely, higher modes (e.g. mode 8) exhibit

Table 2 Parameters of the beam and roving mass

Density ρ	Young's modulus E	Shear modulus G	Poisson's ratio ν	Dimensionless mass τ	Dimensionless rotary inertia φ
7571.43 kg/m^3	188.58GPa	75GPa	0.303	1.15	0.17

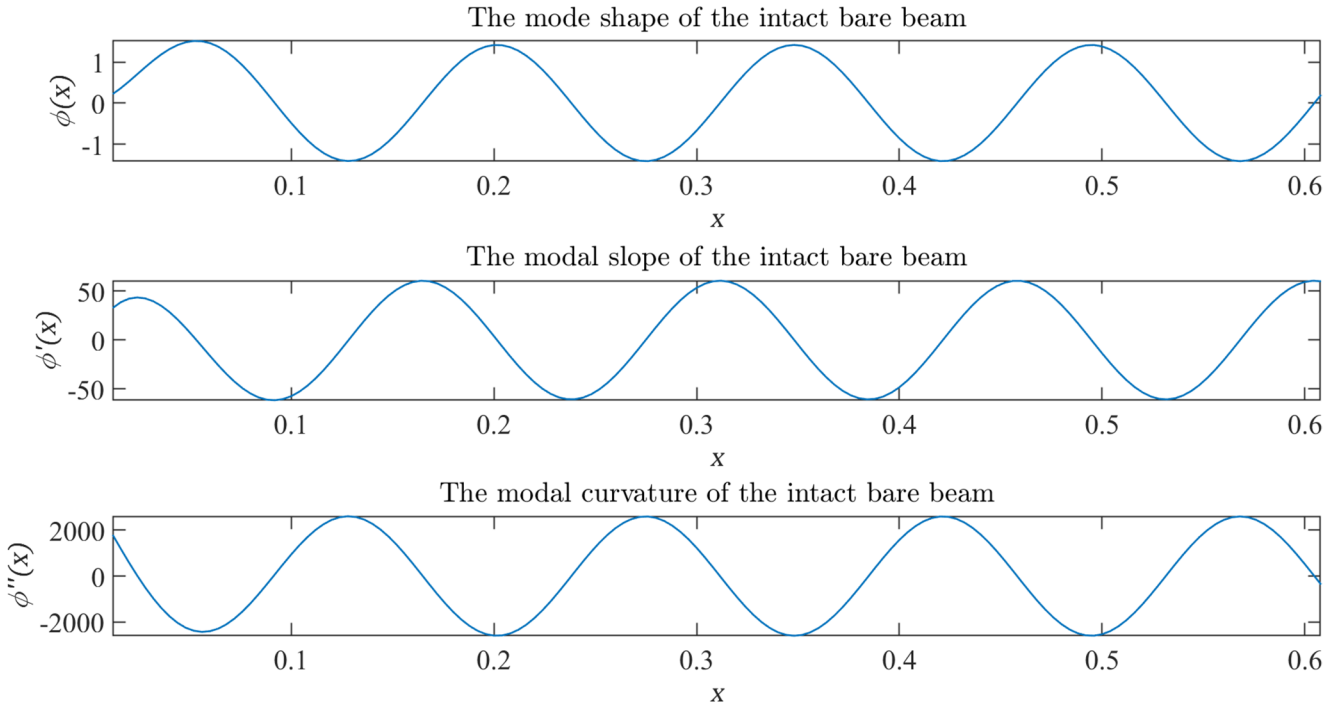

(a) the modal data for the 8th mode of the intact bare beam

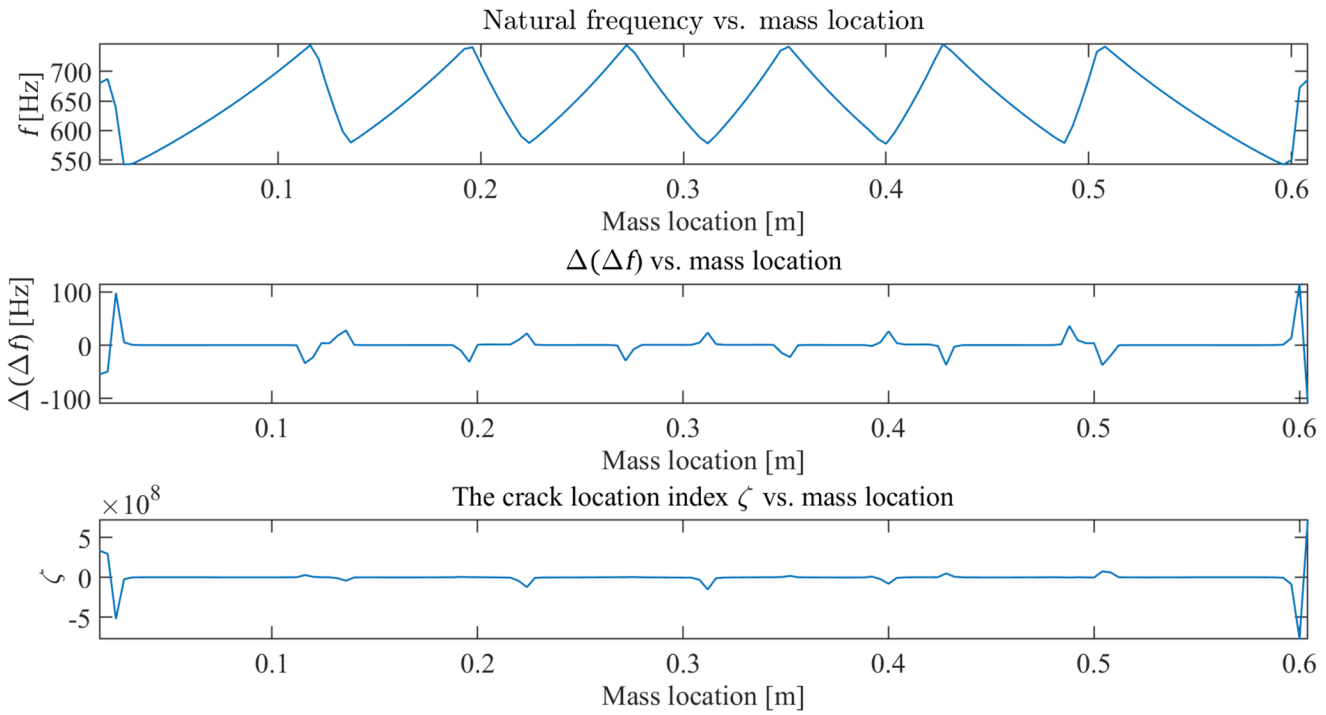

(b) the natural frequency data and ζ for the 8th mode of the cracked beam carrying a roving mass (20% crack at 0.394m)

Fig. 4 The information extracted from the 8th mode. (**a**) the modal data for the 8th mode of the intact bare beam, (**b**) the natural frequency data and ζ for the 8th mode of the cracked beam carrying a roving mass (20% crack at 0.394 m)

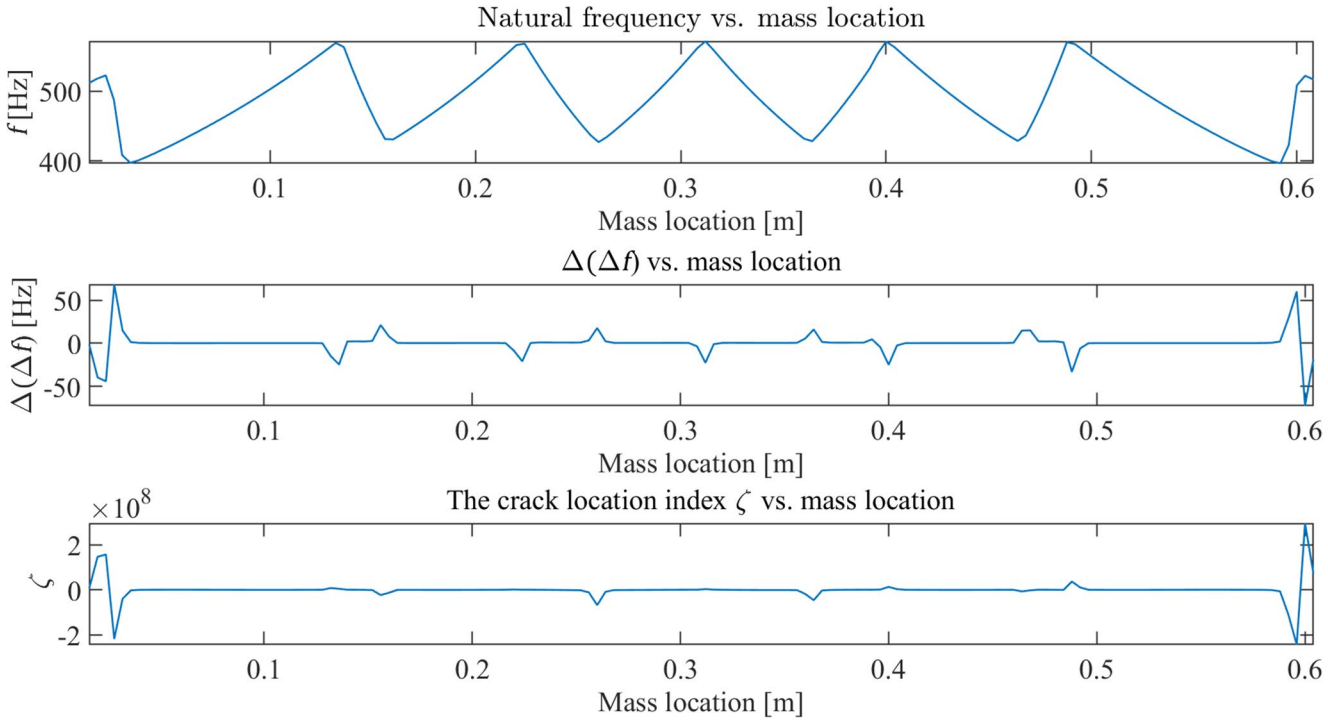

Fig. 5 The natural frequency data and ζ for the 7th mode (20% crack at 0.394 m)

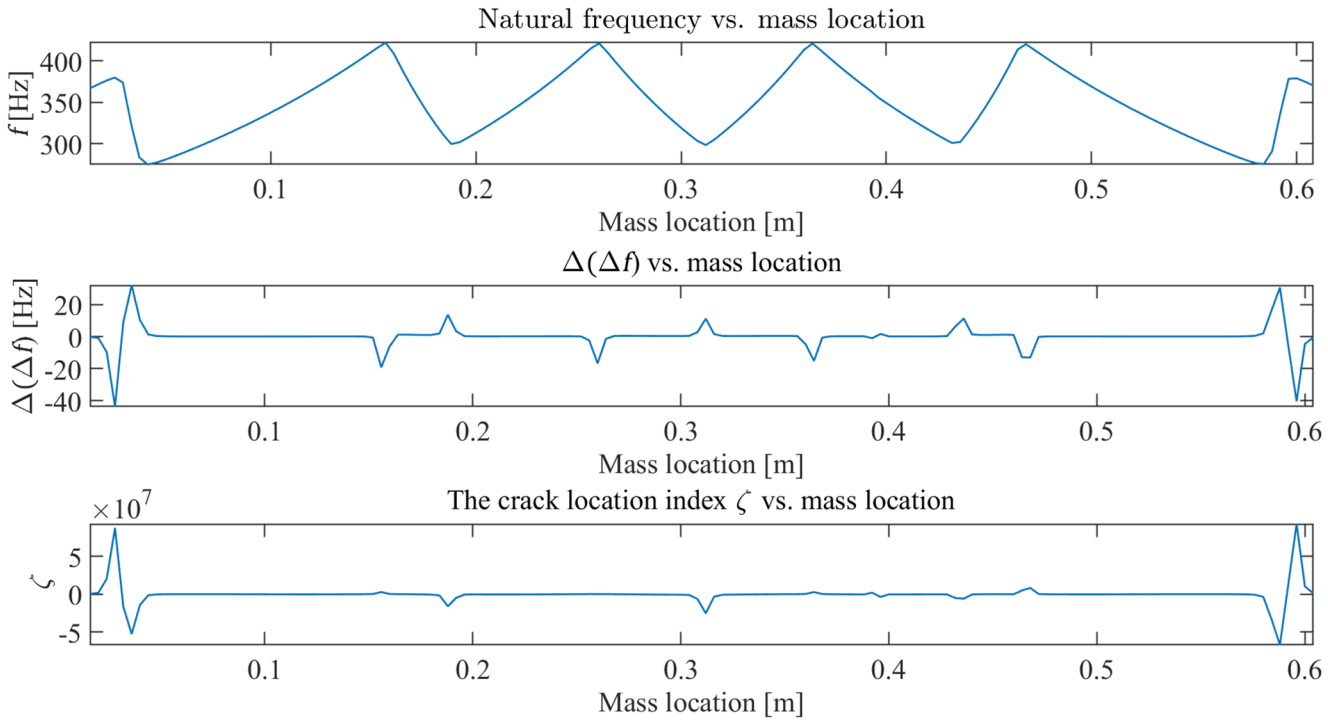

Fig. 6 The natural frequency data and ζ for the 6th mode (20% crack at 0.394 m)

shorter wavelengths and intensified fluctuations in the frequency curve. These fluctuations generate multiple false peaks in $\Delta(\Delta f)$, and although ζ analytically suppresses some of them (as shown in Sect. 2.3), not all false peaks can be removed. As the mode number drops, the modal fluctuations reduce, and fewer false peaks remain unsuppressed after applying ζ. An optimal balance can be reached in the 2nd and 3rd modes where all false peaks except those near

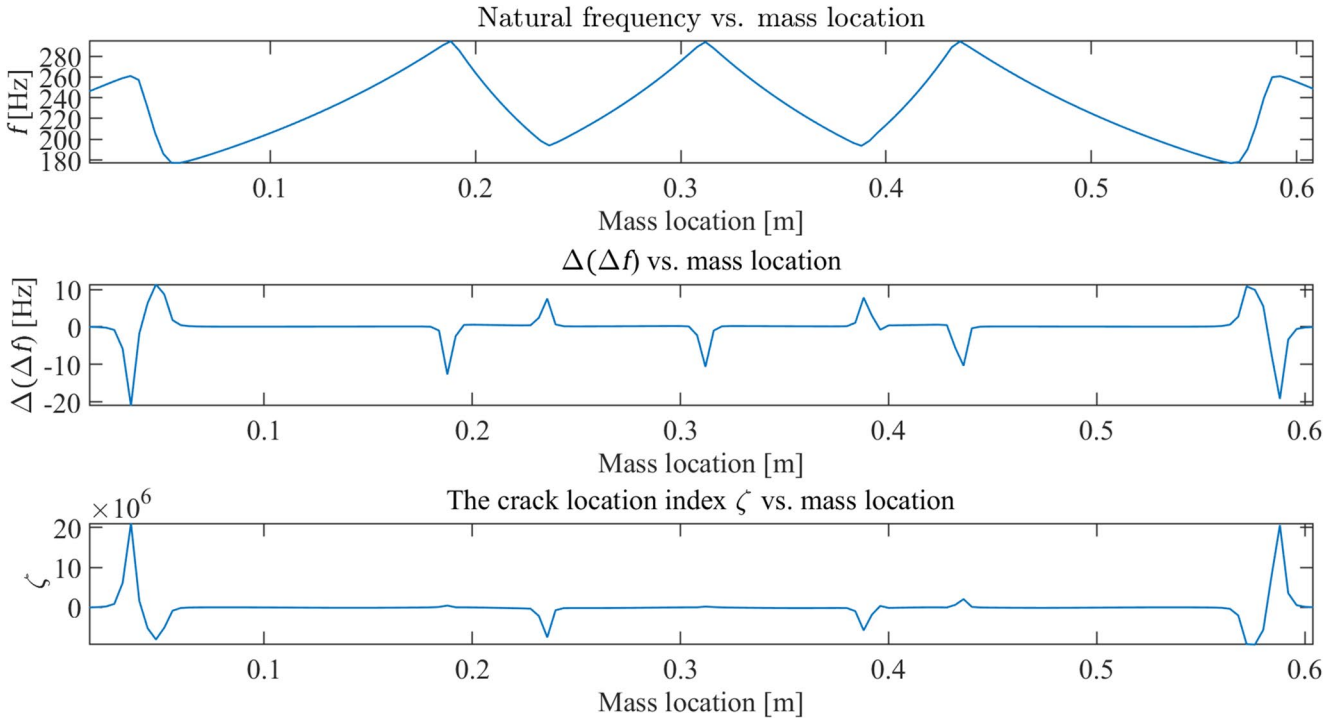

Fig. 7 The natural frequency data and ζ for the 5th mode (20% crack at 0.394 m)

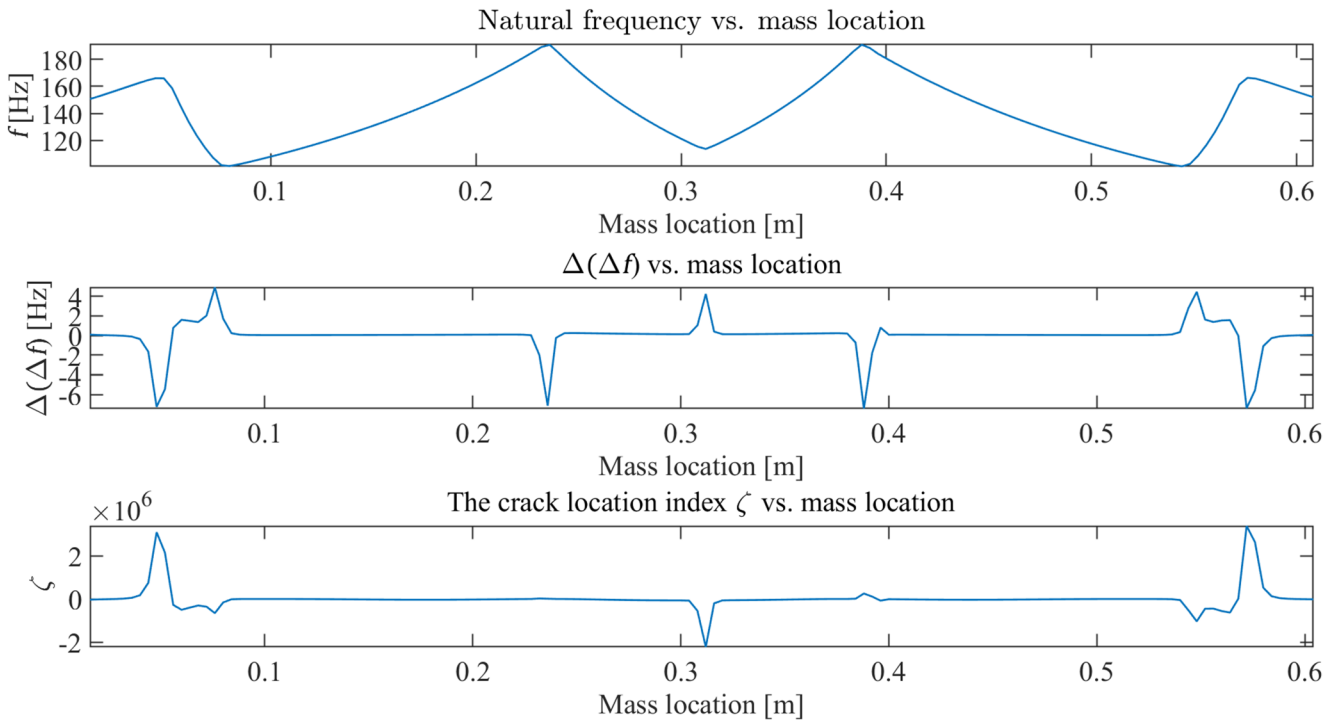

Fig. 8 The natural frequency data and ζ for the 4th mode (20% crack at 0.394 m)

boundaries can be suppressed by ζ, allowing the crack-induced signature to be highlighted.

By only including the results from 0.1 m to 0.5 m, i.e. by excluding the regions near boundaries, the resulting curves of ζ for the first three modes are shown in Fig. 12. These near-boundary regions are excluded because the current index formulation is less reliable near the supports due to strong boundary condition effects, a limitation that is

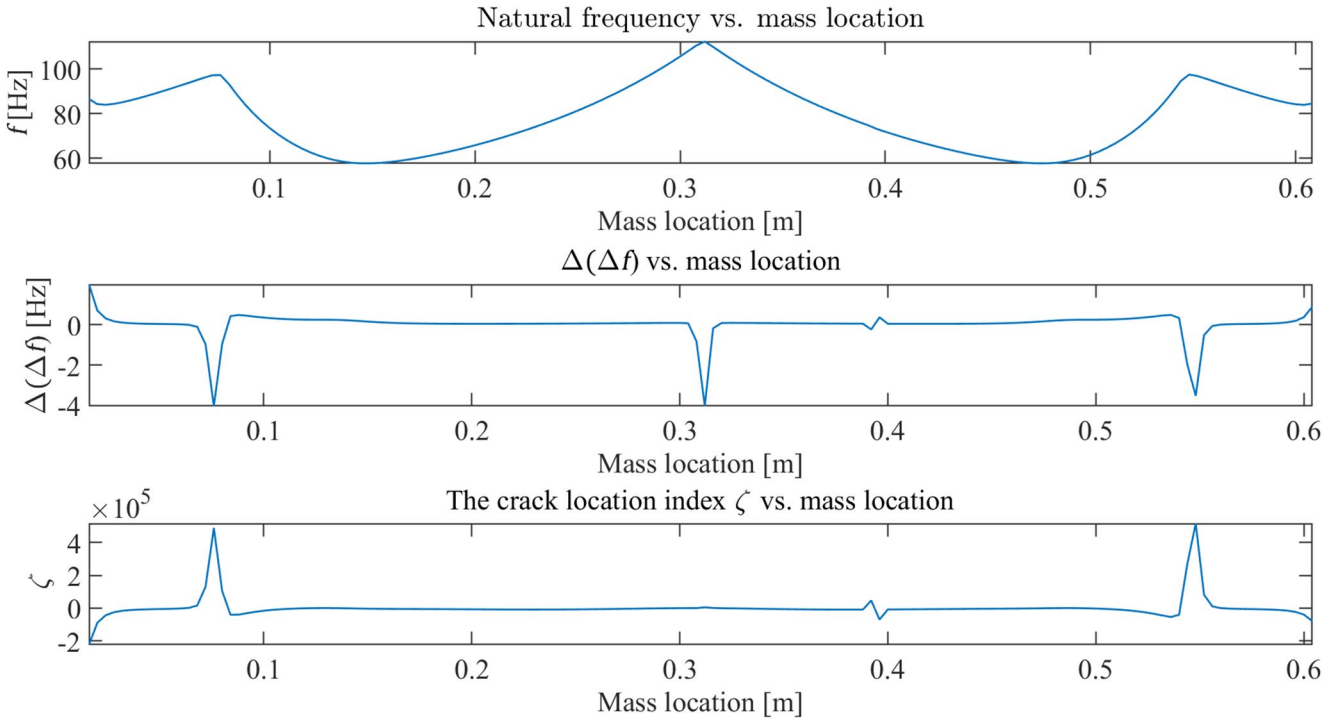

Fig. 9 The natural frequency data and ζ for the 3rd mode (20% crack at 0.394 m)

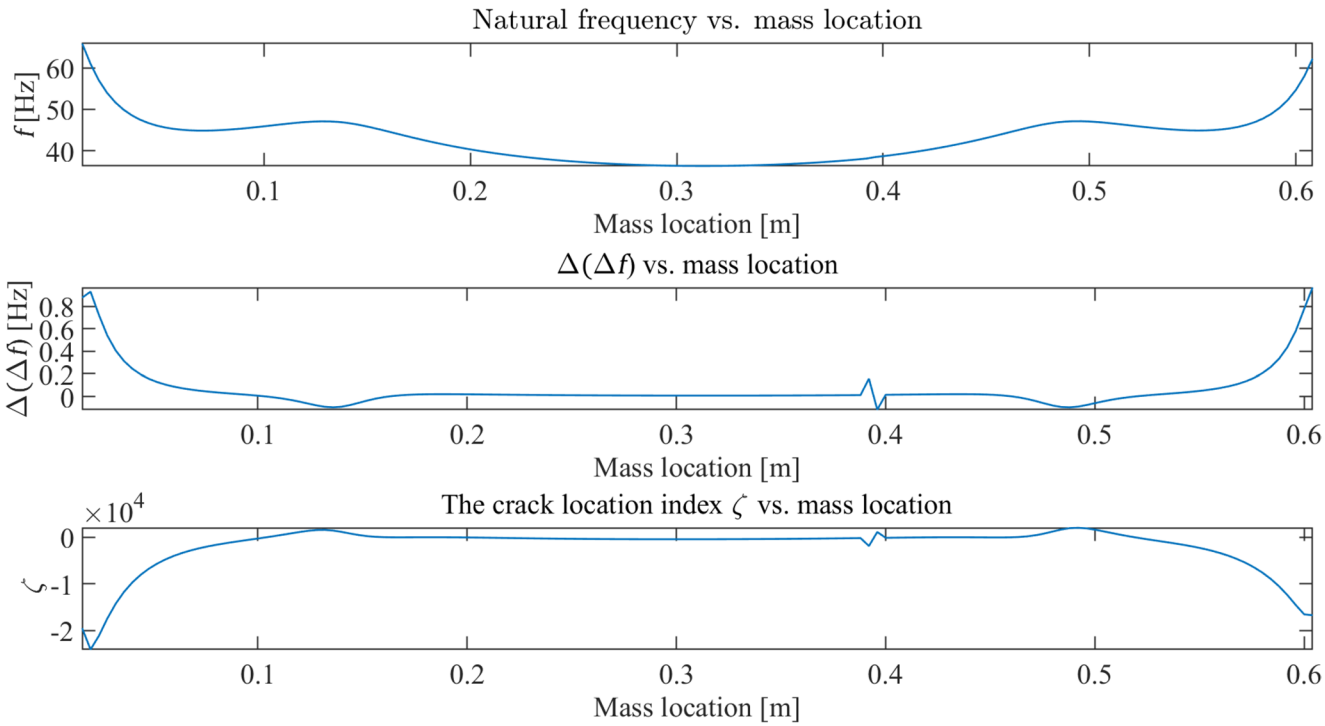

Fig. 10 The natural frequency data and ζ for the 2nd mode (20% crack at 0.394 m)

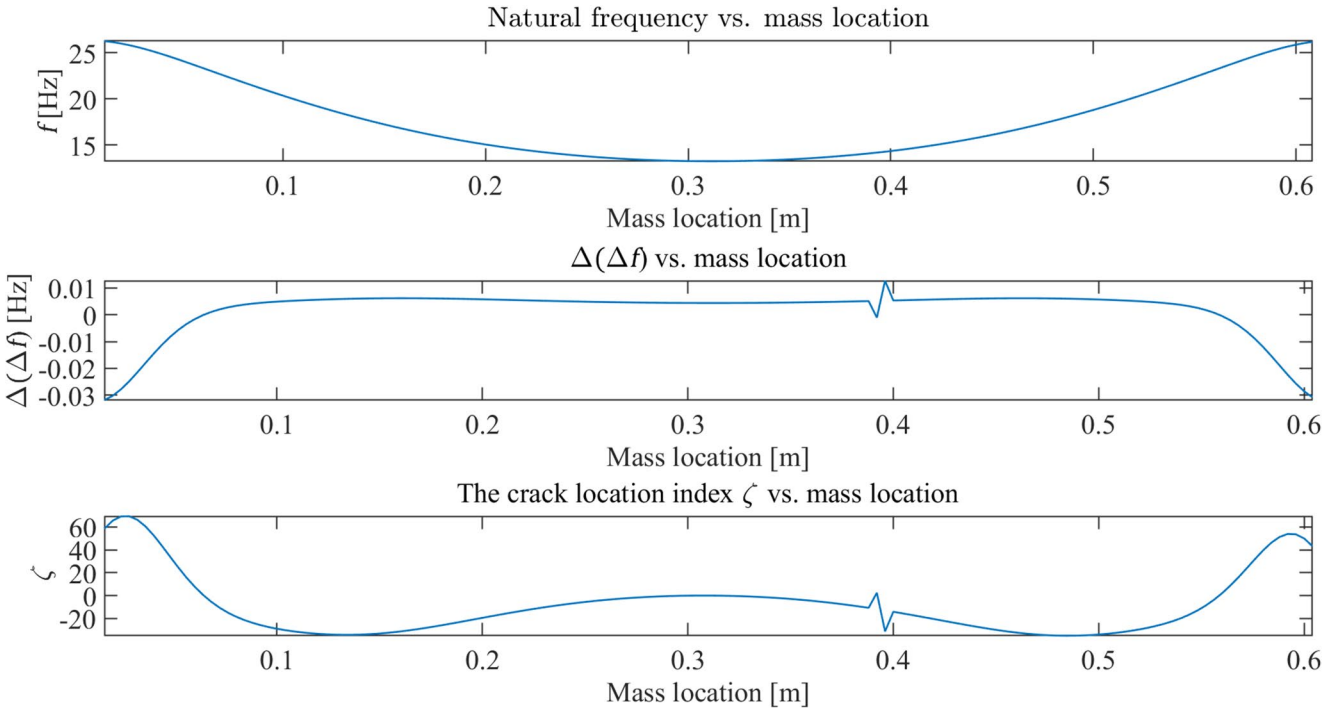

Fig. 11 The natural frequency data and ζ for the 1 st mode (20% crack at 0.394 m)

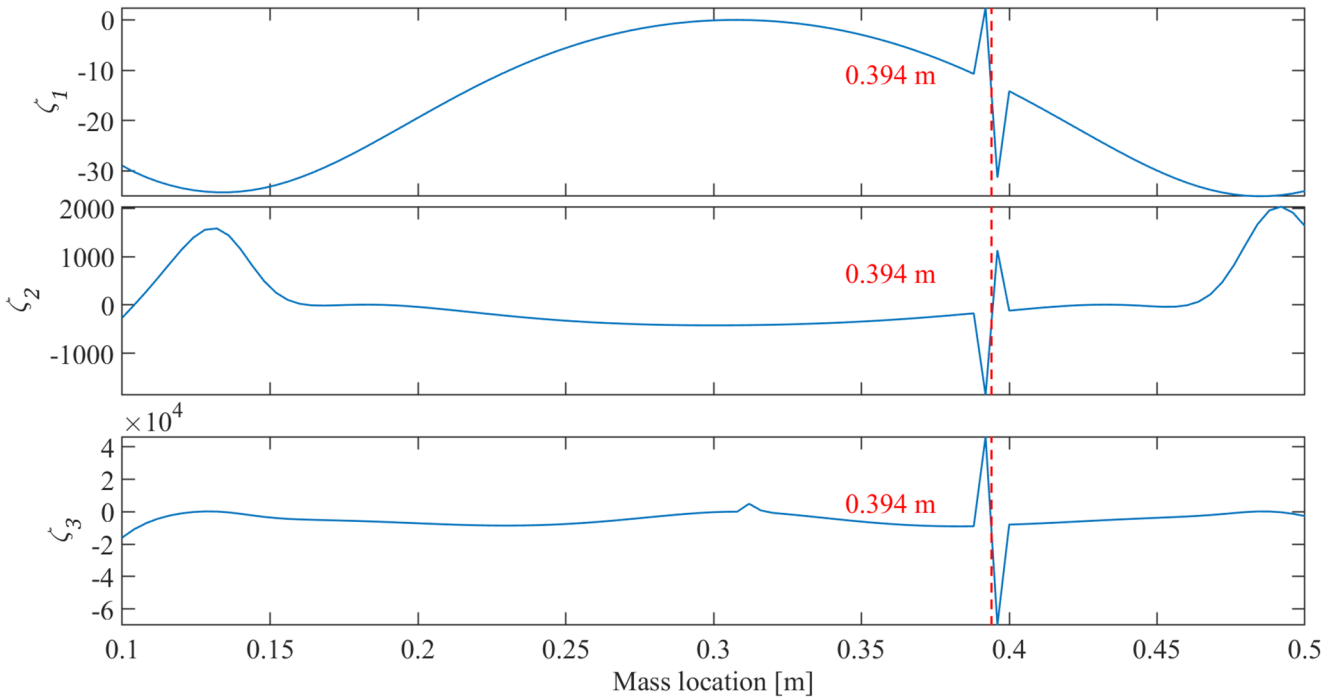

Fig. 12 The curves of ζ_1, ζ_2, and ζ_3 excluding regions near boundaries (20% crack at 0.394 m)

discussed further in the conclusion. From Fig. 12, the location of the 20% crack can be pinpointed from the curves of the crack location index ζ. The average of the x-coordinate of the two prominent peaks (indicated by the red dashed lines in Fig. 12) is taken as the identified crack location, which matches the actual crack location (i.e. 0.394 m).

The Effect of Rotary Inertia and Mass

Based on the DSM model in Sect. 3.1, the effect of the roving rotary inertia on the crack location index for the first 6 modes is shown in Fig. 13. The dimensionless mass τ is maintained as 1.15 and the dimensionless rotary inertia φ varies from 0.03 to 0.17. From Fig. 13, the crack can be clearly identified by the average of the x-coordinate of the two prominent peaks in the first 3 modes. Increasing the rotary inertia helps amplify the peak at the crack location for the first 3 modes. As the mode number increases, additional false peaks remain after applying ζ as previously mentioned, and the curves start to overlap, which means the effect of varying rotary inertia diminishes for higher modes. This agrees with the observation in [30]. Overall, a large rotary inertia would be favourable because the proposed crack location index focuses on lower modes (the 2nd and 3rd modes, specifically) where the effect of varying the rotary inertia is more significant.

Figure 14 illustrates the effect of the roving mass on the crack location index for the first 6 modes. The dimensionless rotary inertia φ is fixed at 0.17 and the dimensionless mass τ varies from 0.38 to 1.15. Compared with varying the rotary inertia, the effect of different mass on the peak at the crack location is less pronounced. For lower modes, a larger mass helps suppress the undulations of ζ curves, thereby highlighting the peak at the crack location. As the mode number increases, more residual false peaks persist after applying ζ, and the influence of varying the mass becomes progressively weaker. Overall, the effect of mass on ζ does not follow a monotonic pattern, thus some trial calculations were conducted when determining the mass in the experiment.

Alternate Crack Locations

This section explores scenarios where the crack is positioned close to the antinodes of the 2nd and 3rd mode shapes of the intact bare beam. In these cases, as the mass passes over the crack, $\phi'_m(x_0)$ (i.e. the slope of the mode shape at the crack location) is close to zero. Consequently, the derived index $\zeta_m(x_0)$ also approaches zero as indicated by Eq. (26), limiting its ability to indicate the crack location. To address this, both the 2nd and 3rd modes are utilized for crack localization. The rationale is that if the crack lies near an antinode of the 2nd mode, $\zeta_2(x_0)$ approaches zero when the mass passes over the crack but $\zeta_3(x_0)$ may still successfully indicates the crack location, and vice versa. The following numerical examples, based on the DSM model in Sect. 3.1, are designed to evaluate this concept by modifying the crack location accordingly.

In the first scenario, the crack is located at 0.442 m where $\phi'_2(x_0)$ is close to zero. The resulting curves of ζ for the first three modes after excluding the regions near boundaries are shown in Fig. 15. From Fig. 15, ζ_2 does not give meaningful results because the peak caused by the mass passing over the crack is also suppressed. In contrast, the peak in the curve of ζ_3 is unaffected and clearly indicates the crack location. The average of the x-coordinate of the two prominent peaks pinpoints the actual crack location (i.e. 0.442 m).

In the second scenario, the crack is located at 0.486 m and thus $\phi'_3(x_0)$ approaches zero when the mass passes the crack. Figure 16 shows the curves of ζ for the first three modes after excluding the regions near boundaries. As illustrated, the curve of ζ_3 does exhibit a distinct peak apart from a minor increase near the beam's midpoint. This small peak is a remnant from the suppression of a more significant peak previously observed in Fig. 9(b). Nevertheless, the crack location remains identifiable through the peak in the curve of ζ_2. The crack location is indicated by the average of the x-coordinate of the two prominent peaks in the ζ_2 curve.

Overall, the combined use of ζ_2 and ζ_3 enhances the reliability of crack localization as the crack-induced peak consistently appears in at lease one of the ζ curves. Even when the peak is attenuated in one mode due to the proximity of a mode shape extremum, it remains distinguishable in the other.

Alternate Boundary Conditions

In this section, the crack location index is evaluated for different boundary conditions. The numerical analysis uses the DSM model in Sect. 3.1, but with altered support configurations. Figure 17 shows the resulting curves of ζ_1, ζ_2, and ζ_3 when the cracked beam is simply supported, clamped-pinned, and clamped-free, respectively. The crack is positioned at 0.394 m as in Sect. 3.1 and results near the boundaries are excluded. Although the boundary conditions vary, distinct peaks consistently emerge in the curves of ζ_2 and ζ_3 as the mass passes over the crack and the crack location can be clearly identified (as indicated by the red dashed lines in Fig. 17), confirming the robustness of the proposed crack location index.

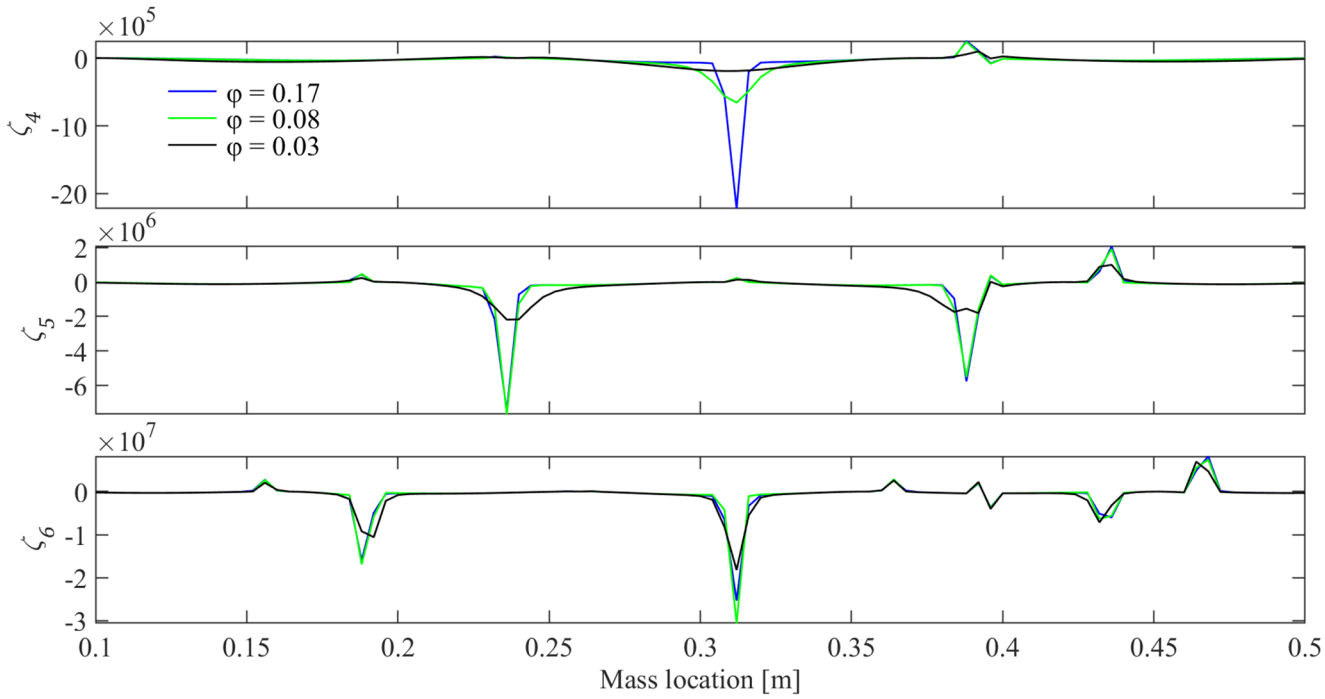

(a) ζ for mode 4, 5, and 6

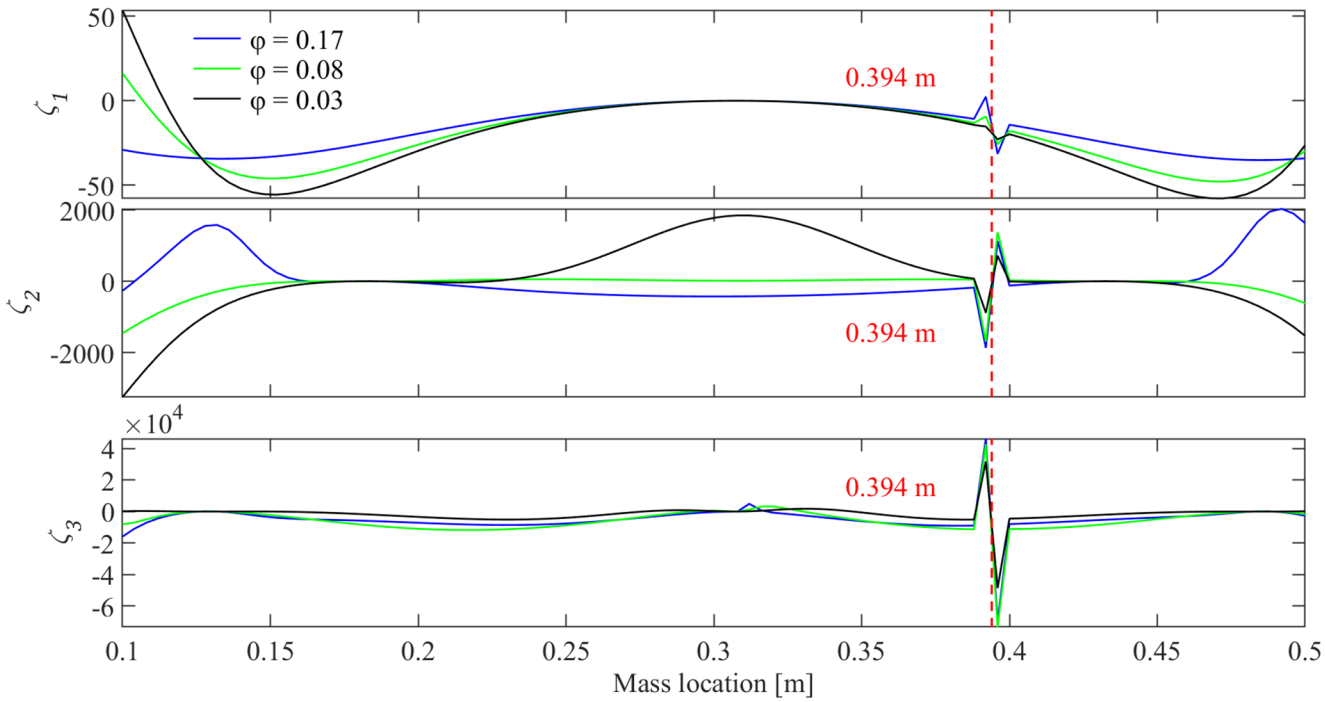

(b) ζ for mode 1, 2, and 3

Fig. 13 The curves of ζ excluding regions near boundaries (20% crack at 0.394 m, $\tau = 1.15$). (**a**) ζ for mode 4, 5, and 6, (**b**) ζ for mode 1, 2, and 3

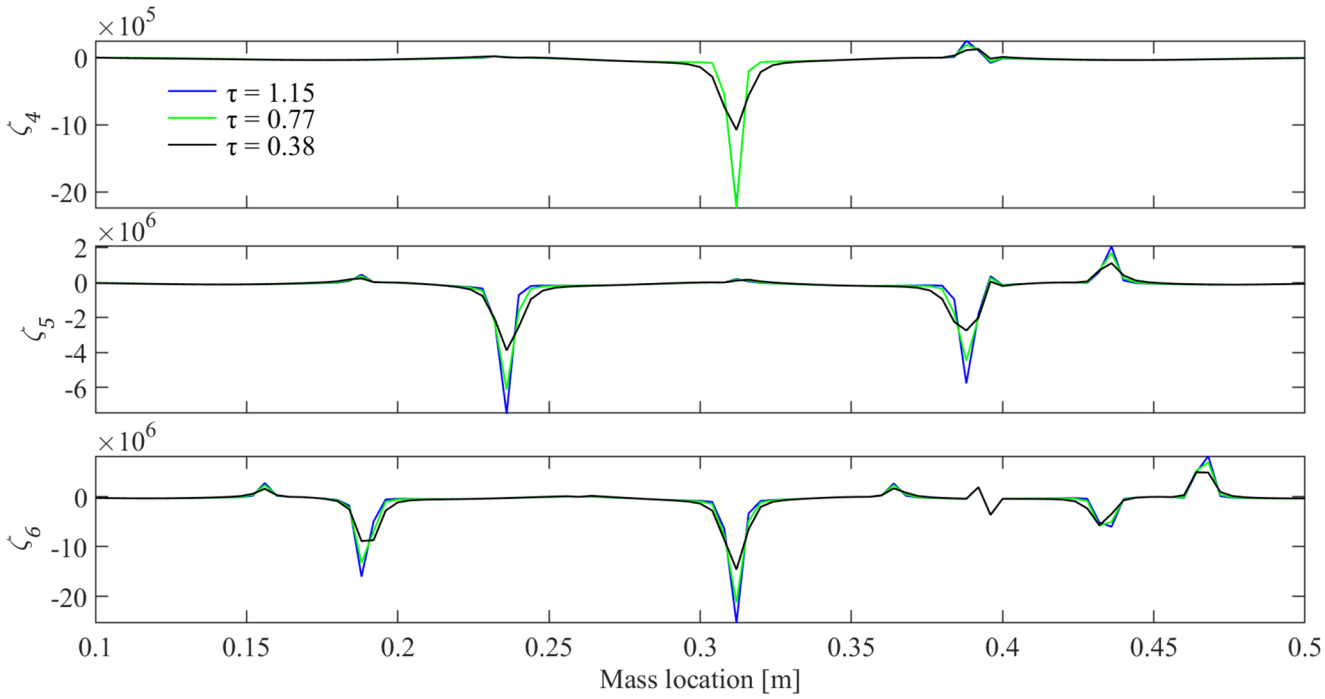

(a) ζ for mode 4, 5, and 6

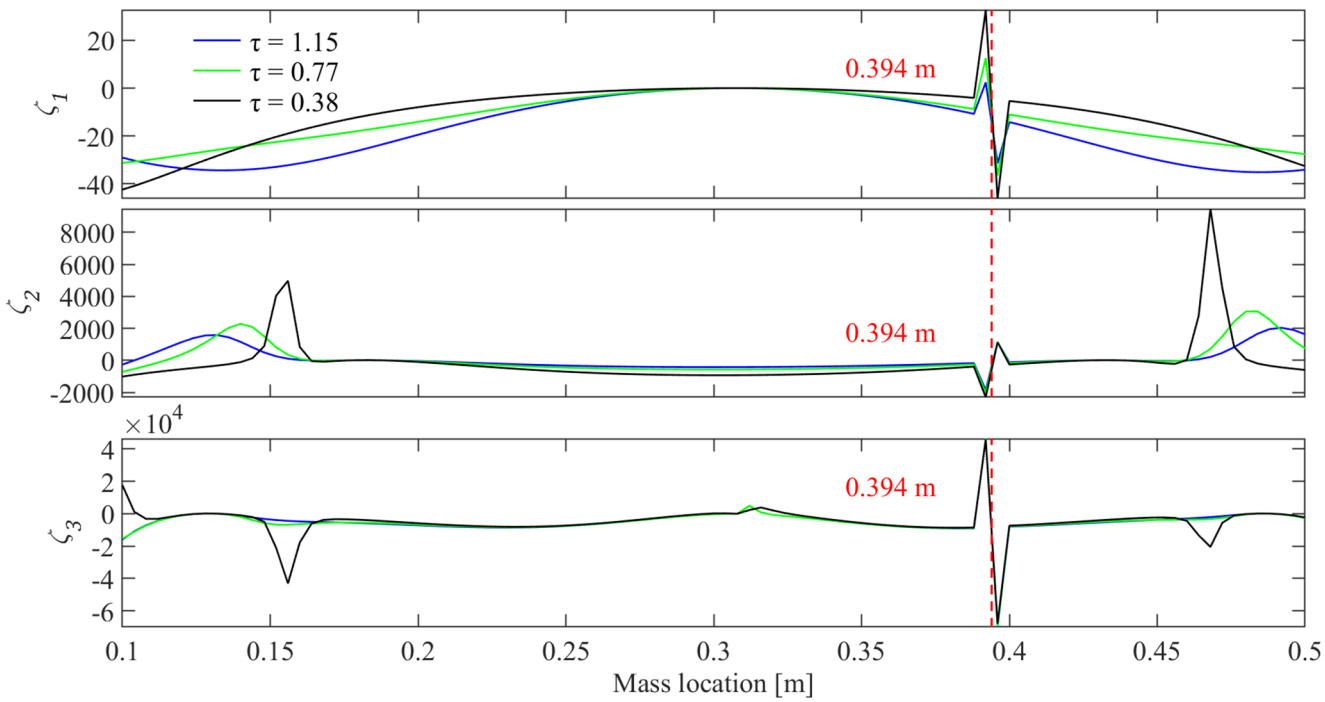

(b) ζ for mode 1, 2, and 3

Fig. 14 The curves of ζ excluding regions near boundaries (20% crack at 0.394 m, $\varphi = 0.17$). (**a**) ζ for mode 4, 5, and 6, (**b**) ζ for mode 1, 2, and 3

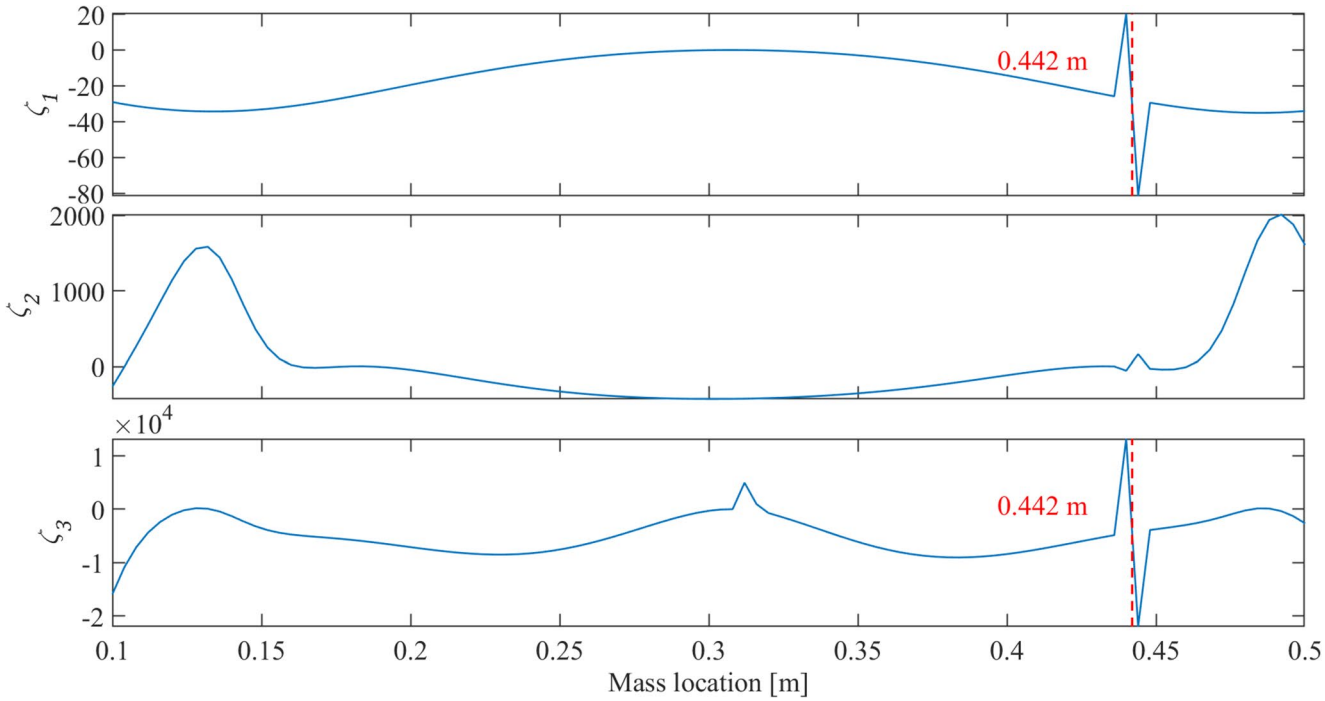

Fig. 15 The curves of ζ_1, ζ_2, and ζ_3 excluding regions near boundaries (20% crack at 0.442 m)

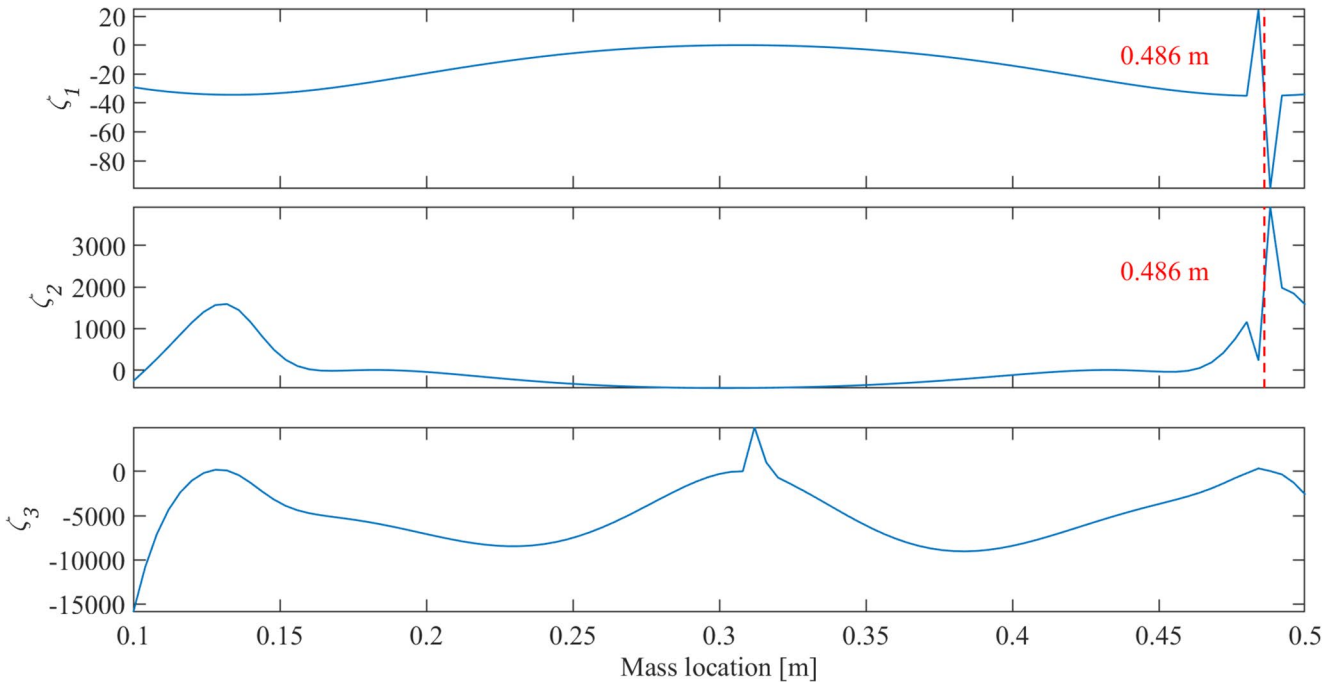

Fig. 16 The curves of ζ_1, ζ_2, and ζ_3 excluding regions near boundaries (20% crack at 0.486 m)

Multi-Crack Scenario

It has been demonstrated in [29] that when a roving mass with rotary inertia passes over multiple cracks on a beam, frequency shifts can be observed at each crack location. Therefore, it is also worth examining whether the proposed crack location index is applicable to multi-crack identification. In this section, the numerical analysis uses the DSM model in Sect. 3.1 with modified crack configurations. Three cases are investigated, each featuring three randomly positioned cracks of 20% severity. The resulting curves of

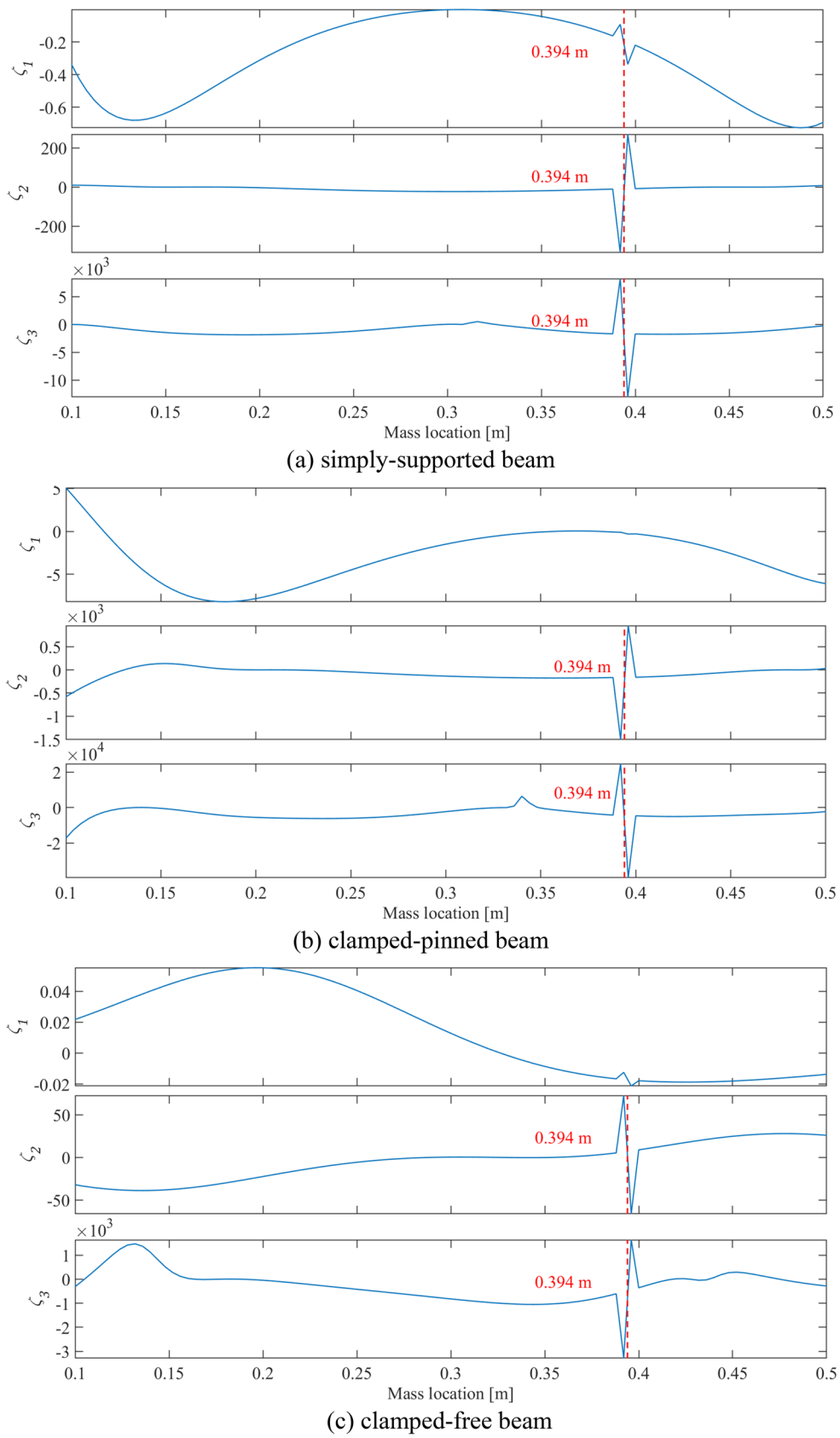

Fig. 17 The curves of ζ_1, ζ_2, and ζ_3 for different boundary conditions (20% crack at 0.394 m). (**a**) simply-supported beam, (**b**) clamped-pinned beam, (**c**) clamped-free beam

ζ for the first three modes after excluding the regions near boundaries are shown in Fig. 18.

Figure 18 shows that cracks can be clearly identified by the peaks in ζ_2 and ζ_3. Although the magnitude of peaks may vary among different modes, and some crack-induced peaks may be suppressed when the crack lies near an antinode (as discussed in Sect. 3.3), the combined use of ζ_2 and ζ_3 ensures that there is at least one distinguishable peak at each crack location, preventing missed identifications.

It should be noted that the present index is developed for open cracks and a single roving mass; scenarios involving asymmetric damage or more complex mass distributions introduce additional dynamic interactions and are therefore identified as directions for future work.

Experimental Validation

This section outlines the experimental set-up for investigating the existence and measurability of the natural frequency shift when a roving mass with rotary inertia is shifted across a crack. Experimental results from the 20% cracked beam carrying a roving mass with the maximum rotary inertia setting are presented here. Results from both the 20% and 40% cracked beams are used to verify the crack location index.

Experiment Layout

The experimental set-up is shown in Fig. 19. A heavy steel platform with two supports was designed to carry a beam. The beam made of mild steel was clamped to the support at both ends. A crack was introduced by machining a flat-bottomed notch 2 mm wide on the beam. Two crack depths were used, corresponding to 20% and 40% thickness reduction of the beam, respectively.

The roving mass was made of steel and was clamped to the beam with fasteners. The roving mass is 1.15 times the mass of the beam, equal to one of the dimensionless mass values in Sect. 3.2. The rotary inertia of the roving mass can be adjusted by changing the radius of gyration (see Fig. 20). Impact hammer tests were performed whenever the mass was located in a new position to measure the frequency response of the set-up. The spacing for roving mass placement was 4 mm. A total of 71 mass locations within a range of 280 mm were tested on each cracked beam. The coordinate of the centre of the crack was 394 mm from the left end. For each cracked beam, three settings of rotary inertia as shown in Fig. 20 were tested, corresponding to the three magnitudes of rotary inertia tested in Sect. 3.2.

Natural Frequency Extraction

During the impact hammer tests, the excitation and response signals were processed by a dynamic signal analyser (model: Data Physics QUATTRO) which gave the transfer function. SignalCalc 900 Series software was used to configure the signal analyser and visualize the signals. The data files containing the transfer function signal were then exported to MATLAB for natural frequency extraction. Figure 21 shows a typical plot of the accelerance frequency response function (FRF) measured on the 20% cracked beam carrying the roving mass with the maximum rotary inertia setting, when the distance between the mass location and the left end of the beam is 0.256 m. The magnitude plot (top) highlights multiple resonance peaks over the 0–800 Hz frequency range, while the phase plot shows the expected 180° phase transitions across each natural frequency. The sharp resonance peaks indicate the light damping of the system.

The process of natural frequency extraction consists of curve-fitting a theoretical expression for how an FRF behaves near resonance. This is required because the FRF is measured at discrete frequency points and the measured resonance peak does not necessarily align with the true resonance frequency (see Fig. 22). The single-degree-of-freedom (SDOF) circle-fit method was employed to improve the accuracy of natural frequency estimation. This method works adequately for structures whose frequency response functions exhibit well-separated modes which are lightly damped [42]. It is based on the fact that, for the general SDOF systems, a Nyquist plot of the frequency response properties produce a circle-like curve (an exact circle if the appropriate parameter is chosen for the type of damping model), and on the fact that multi-degree-of-freedom (MDOF) systems produce Nyquist plots of frequency response data which include sections of near-circular arcs corresponding to the regions near the natural frequencies [42]. As an example, the resonance highlighted in the magnitude and phase plots (Fig. 21) corresponds to a natural frequency near 383 Hz. Due to the discrete frequency resolution of the measured FRF, the peak magnitude does not necessarily coincide with the true resonance frequency. To improve accuracy, the complex-valued FRF data in the vicinity of this peak are plotted in the Nyquist plane (see Fig. 23), where lightly damped SDOF behaviour produces a near-circular arc. A least-squares circle fit is then applied, yielding an accurate estimate of the natural frequency (383.08 Hz). Together, Figs. 21 and 23 illustrate both the identification of the resonance from the FRF and the refined estimation enabled by the circle-fit method.

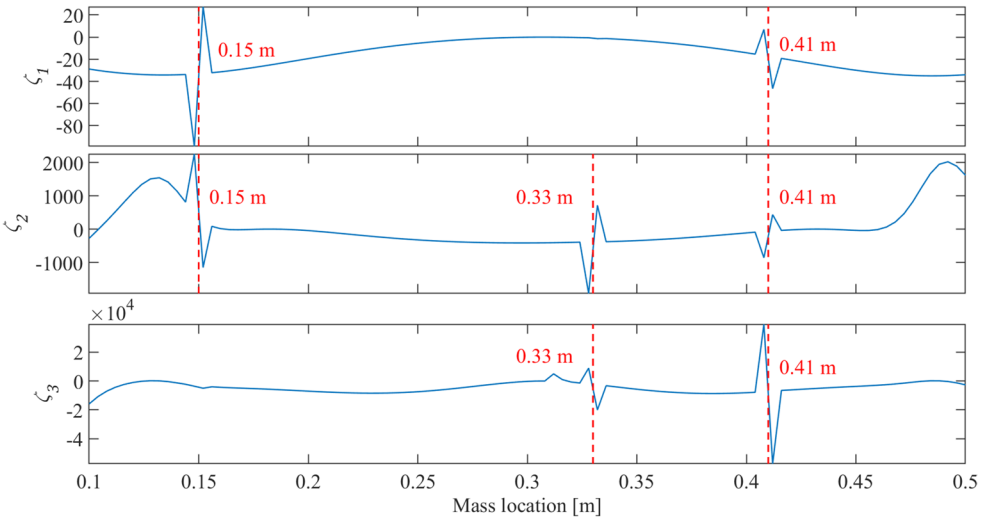

(a) case 1: cracks are located at 0.15m, 0.33m, and 0.41m

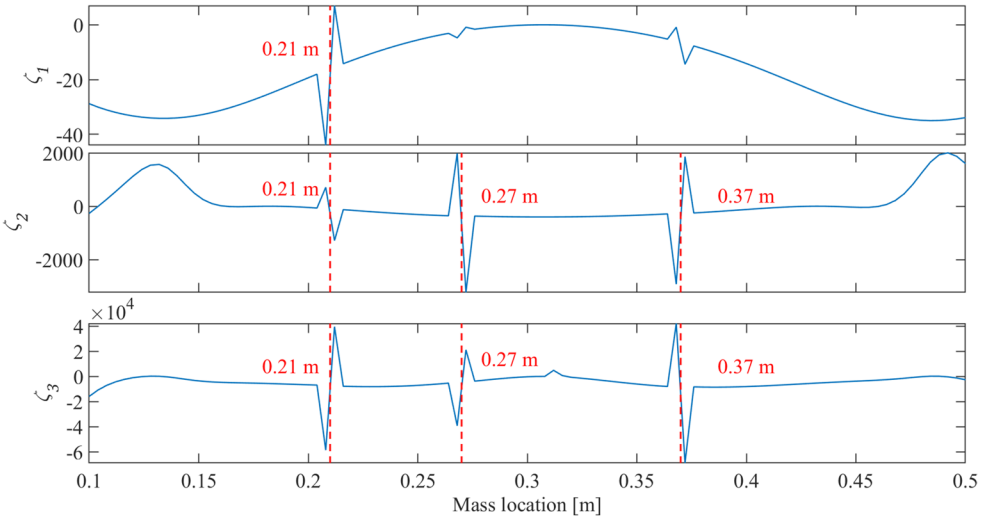

(b) case 2: cracks are located at 0.21m, 0.27m, and 0.37m

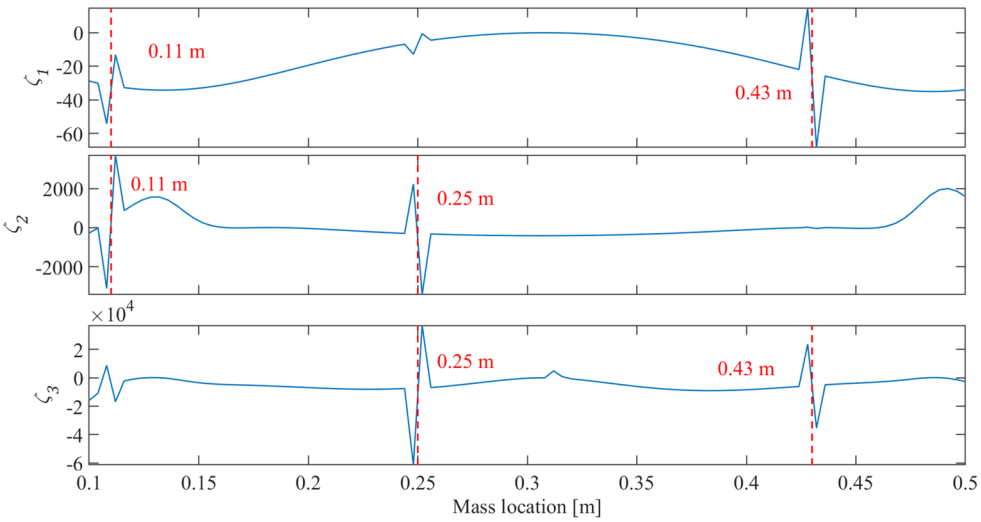

(c) case 3: cracks are located at 0.11m, 0.25m, and 0.43m

Fig. 18 The curves of ζ_1, ζ_2, and ζ_3 for multi-crack cases (excluding regions near boundaries, all cracks are 20%). (**a**) case 1: cracks are located at 0.15 m, 0.33 m, and 0.41 m, (**b**) case 2: cracks are located at 0.21 m, 0.27 m, and 0.37 m, (**c**) case 3: cracks are located at 0.11 m, 0.25 m, and 0.43 m

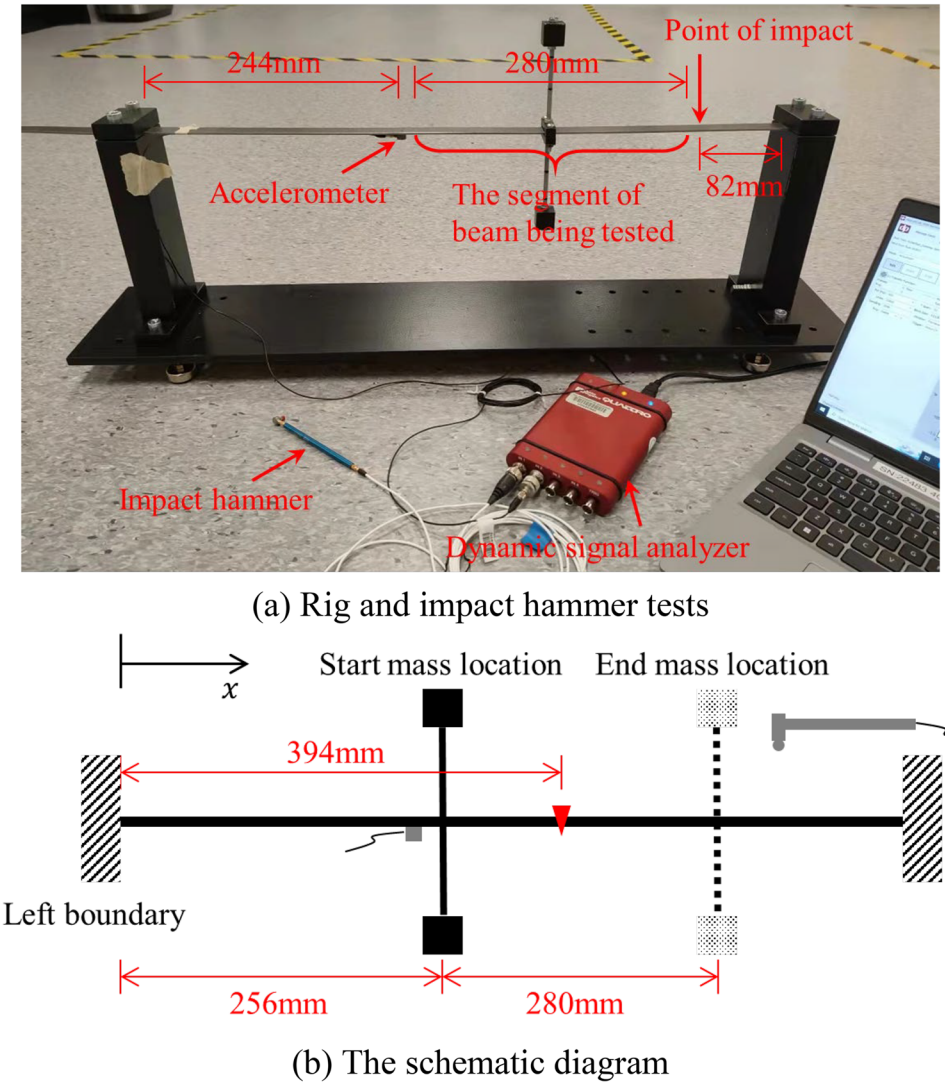

Fig. 19 The experimental set-up. (**a**) rig and impact hammer tests, (**b**) the schematic diagram

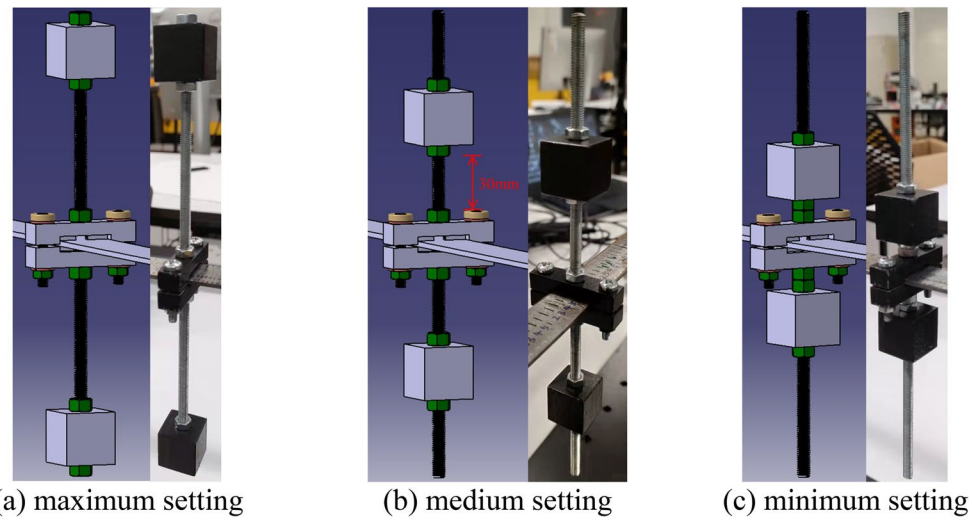

Fig. 20 Different settings of the rotary inertia (design figures and photos) [32]. (**a**) maximum setting, (**b**) medium setting, (**c**) minimum setting

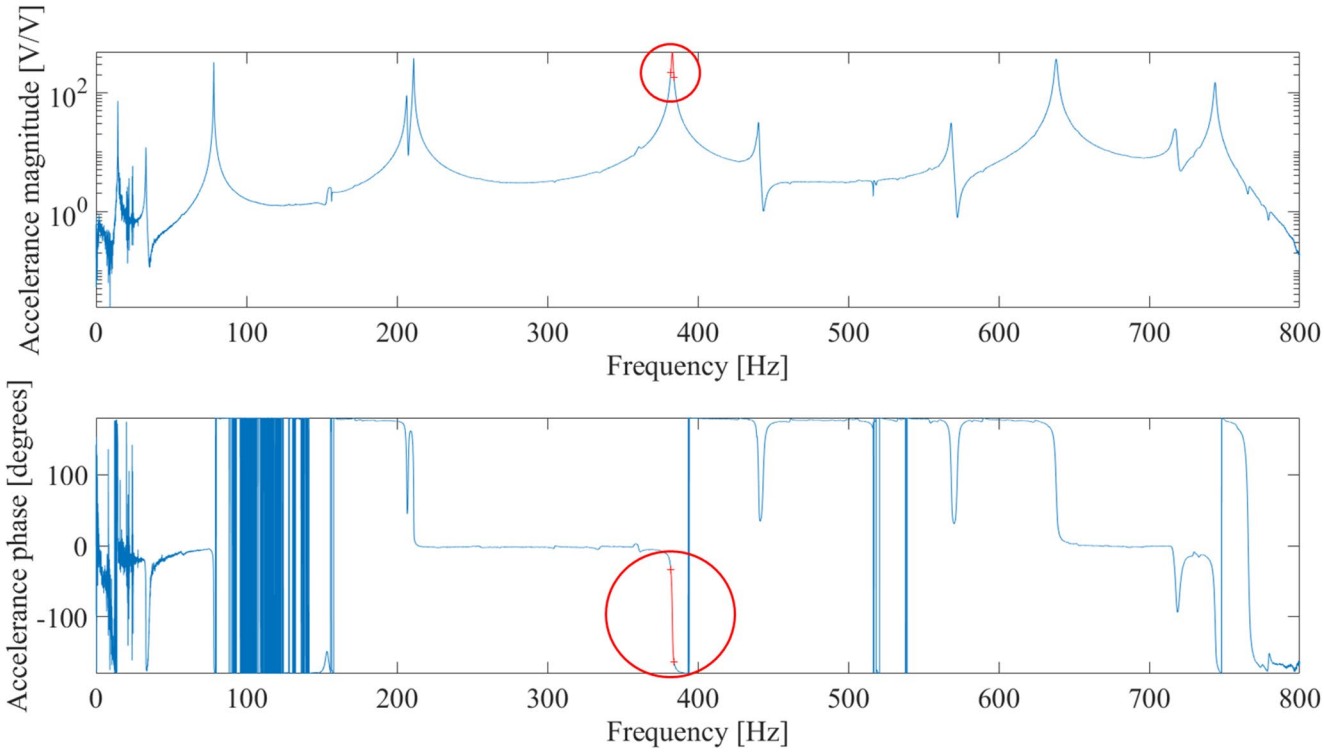

Fig. 21 Measured accelerance FRF showing the magnitude (top) and phase (bottom) over the 0–800 Hz frequency range

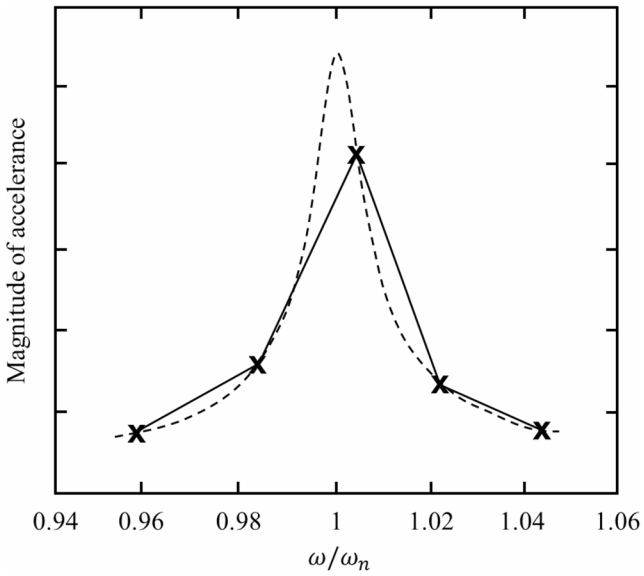

Fig. 22 A typical resonance peak ('x' indicates discrete data points)

20% Cracked Beam Results

The natural frequency results for the 20% cracked beam carrying a roving mass with the maximum rotary inertia setting are shown in Fig. 24. The experimental results are also compared with those obtained using ANSYS simulations and the analytical DSM model. The results from different methods are in good agreement. The average relative percentage error between experimental results and ANSYS results for the first eight natural frequencies is between 2.47% and 8.17%. To confirm the measurability of the frequency changes when the roving mass passed the 20% crack in the presence of measurement noise and small parameter variations, a measurability check has been presented in Appendix B. The natural frequency shift that occurs when the mass passes the crack at 394 mm is measurable, but it is not easily distinguishable from the overall natural frequency curve. In addition, irregular frequency variations elsewhere in the data may further obscure this effect and make visual interpretation more challenging. For example, some abnormal frequency shifts appear in the curves of the 4th and 5th natural frequencies because these two modes are closely coupled with two modes in other directions (see Fig. 25), respectively, when the mass is located at certain locations (approximately 4 mass locations in the 4th natural frequency and 5 mass locations in the 5th natural frequency).

The comparison of the results of natural frequency shift Δf is made in Fig. 26. For the Δf curve, the peak corresponding to the crack location is relatively small at lower frequencies. For example, it is impossible to find a noticeable peak at the crack location for the 1 st natural frequency. For the 2nd natural frequency, the peak at the crack location is observable, however, the magnitude of the peak is comparable to that of the peak caused by a measurement error. False peaks appear in the curves of Δf of the 4th

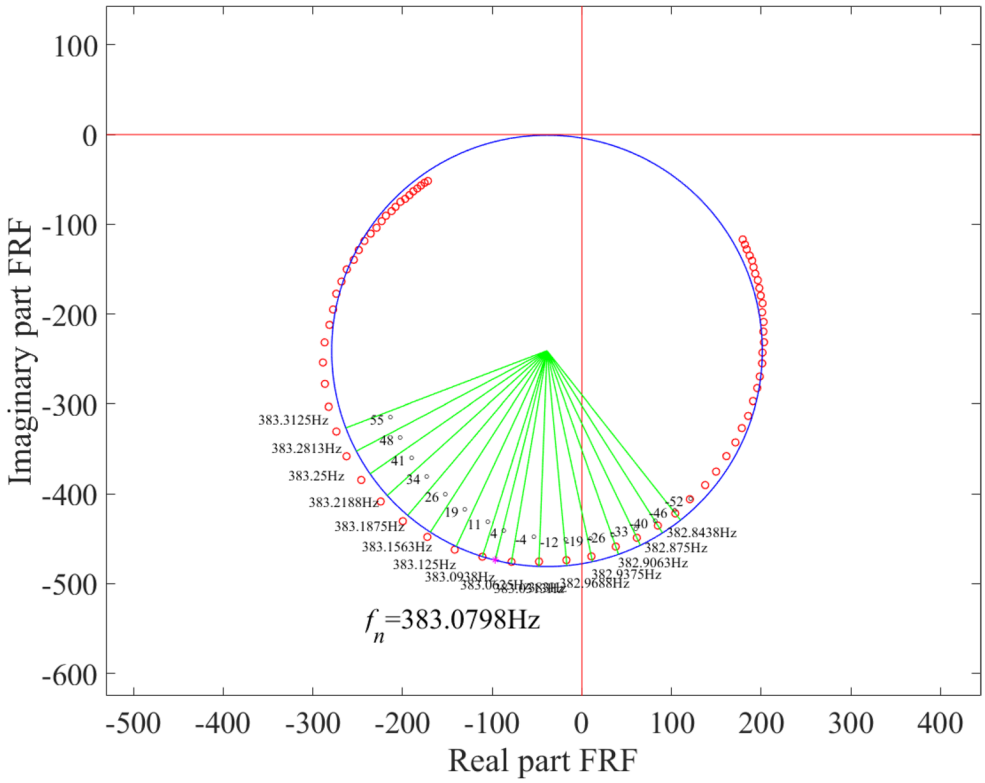

Fig. 23 Nyquist plot of the complex-valued accelerance FRF in the vicinity of the resonance as highlighted in Fig. 21

and 5th natural frequencies due to closely coupled modes. For the 6th to 8th natural frequencies, the curves exhibit intensified fluctuations, making the crack-induced peak less discernible.

Although the natural frequencies f for the 2nd and 3rd modes show good agreement with the ANSYS and DSM predictions (Fig. 24), the corresponding Δf curves exhibit noticeably stronger oscillations (Fig. 26(b, c)). This behaviour occurs because Δf is obtained by differencing two natural frequency measurements at adjacent mass locations, effectively acting as a numerical derivative of the measured f-curve. Even small experimental variations (e.g. slight differences in hammer excitation, bolt-tightening torque variations when repositioning the mass, or minor errors in mass placement) are amplified in the differenced quantity, despite being barely visible in the underlying frequency values.

To reduce the fluctuations, the curves of $\Delta(\Delta f)$ are shown in Fig. 27. For the $\Delta(\Delta f)$ curve, the overall profile is flatter and the peak at the crack location appears more pronounced. However, the presence of false peaks hinders reliable crack localization. These false peaks are generally due to measurement error or the small natural frequency shift around the extrema of the natural frequency curve. For the 1 st mode, the crack-induced frequency shift is relatively small and of the same order as the combined measurement uncertainty. Therefore, neither Δf nor $\Delta(\Delta f)$ yields a reliable crack signature for the 1 st mode, as shown in Fig. 26(a) and Fig. 27(a). As an example, Fig. 28 presents the results of the 8th natural frequency, where Δf changes in sign near the extrema of the f curve, leading to additional peaks in the $\Delta(\Delta f)$ curve, which agrees with the observation in Fig. 4. These additional peaks are comparable in magnitude to the peak associated with the crack, thereby preventing clear identification of the crack location.

Implementation of the Crack Location Index

To suppress the additional peaks, the crack location index is applied to the 3rd natural frequency. Figure 29 shows the curves of f_3, $\Delta(\Delta f_3)$, and ζ_3 for three different settings of the rotary inertia. When the rotary inertia is set to the maximum and medium values, the crack location is indicated by the most significant change in the curve of ζ_3. When the rotary inertia is at the minimum setting, a noticeable variation in ζ_3 is still observed near the actual crack location. The average of the x-coordinate of the two prominent peaks is taken as the identified crack location, which is 0.394 m for both the maximum and medium rotary inertia settings, and 0.386 m for the minimum rotary inertia setting. The maximum distance between the actual crack location (i.e. 0.394 m) and the identified crack location is 8 mm. Overall, the crack location can be accurately identified using the proposed index. Furthermore, ζ_3 exhibits a smoother profile compared with $\Delta(\Delta f_3)$, which is beneficial for determining the crack location.

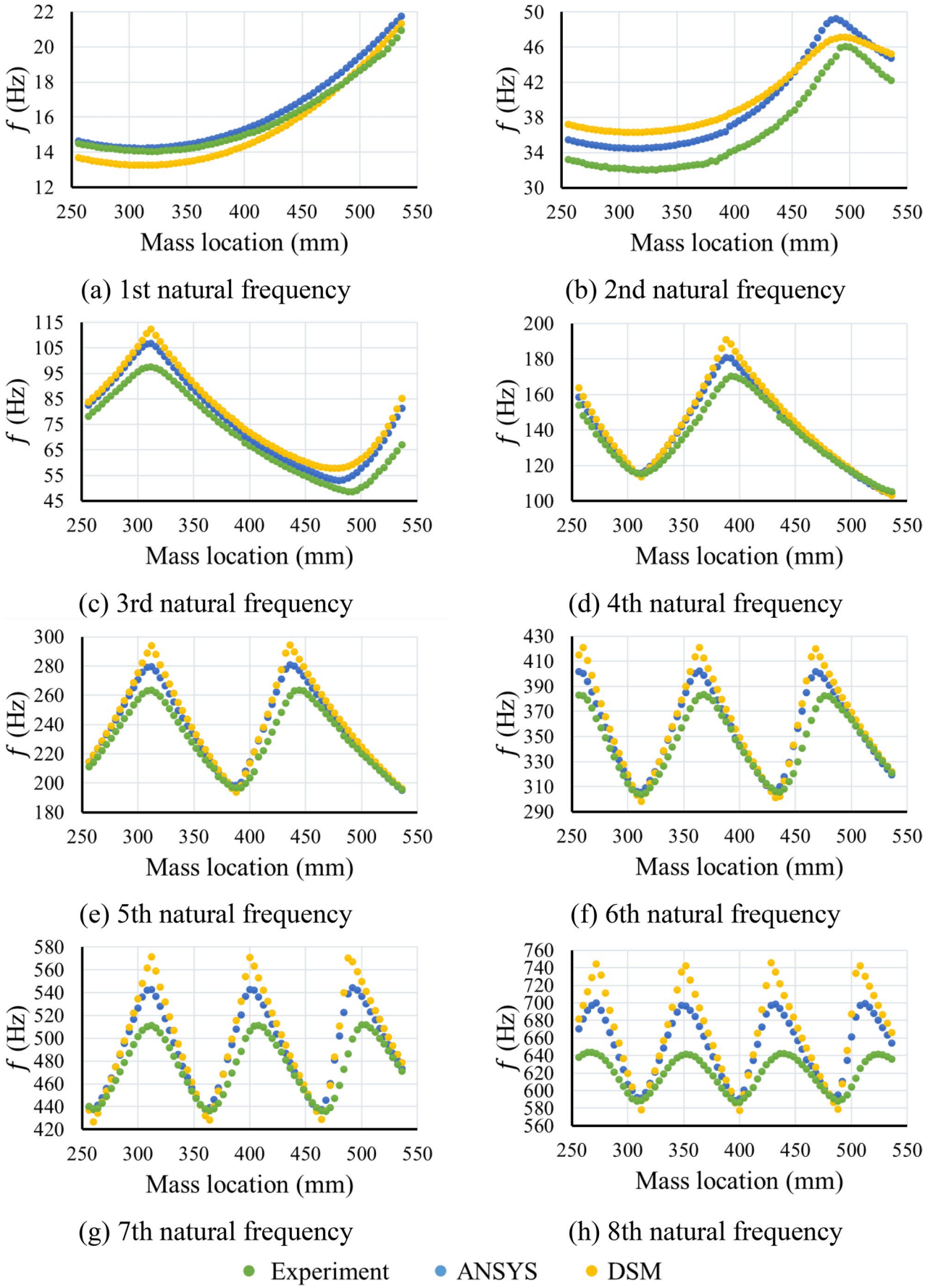
f (Hz)
Mass location (mm)
(a) 1st natural frequency
(b) 2nd natural frequency
(c) 3rd natural frequency
(d) 4th natural frequency
(e) 5th natural frequency
(f) 6th natural frequency
(g) 7th natural frequency
(h) 8th natural frequency
Experiment
ANSYS
DSM

Fig. 24 The comparison of natural frequency results (20% crack at 394 mm). (**a**) 1 st natural frequency, (**b**) 2nd natural frequency, (**c**) 3rd natural frequency, (**d**) 4th natural frequency, (**e**) 5th natural frequency, (**f**) 6th natural frequency, (**g**) 7th natural frequency, (**h**) 8th natural frequency

To further verify the applicability of the crack location index, it is also applied to the experimental data from the 40% cracked beam. The resulting curves are presented in Fig. 30. While the $\Delta(\Delta f_3)$ plots already provide sufficient information to identify the crack location, the curves of ζ_3 offer a smoother representation. This smoothness enhances the visibility of the abrupt change in ζ_3 as the mass passes over the crack, thereby facilitating clearer crack localization. The crack is consistently identified at 0.394 m, which matches the actual crack location accurately.

Overall, when the crack is relatively severe, the crack location can be identified from the pronounced peak in the curve of Δf or $\Delta(\Delta f)$ versus mass location. However, in the presence of a small crack, the occurrence of false peaks in the curve of $\Delta(\Delta f)$ may impede the determination of crack location. Under such conditions, the proposed crack location index ζ offers improved performance as it effectively attenuates some of the false peaks and enhances the identifiability of the crack location.

Concluding Remarks

In this study, an analytical formulation was developed to estimate the natural frequencies of an Euler-Bernoulli beam subjected to a roving mass with rotary inertia. The derived expression was validated against results obtained from the Dynamic Stiffness Method (DSM). Leveraging this formulation, a crack location index ζ (i.e. Equation (26)) was proposed and analytically justified. A key advantage of the proposed index is its ability to suppress false peaks in the curve of $\Delta(\Delta f)$ (i.e. the change of natural frequency shift when a stationary mass traverses the beam, as defined in Eq. (25)) for the lower modes, thereby highlighting the true peak corresponding to the crack location. In addition, ζ can be calculated using only the measured natural frequencies of the cracked beam and standard modal data for intact beams available in the literature for common boundary conditions. To assess its robustness, numerical studies were performed using DSM-based models with variations in rotary inertia and mass, crack location (including near modal antinodes), and boundary conditions (simply supported, clamped, and cantilever). The applicability of ζ for multi-crack identification was also investigated. The results demonstrate that when the 2nd and 3rd modes are used, cracks are consistently identified from the peaks of ζ curves with high accuracy. Experimental verification using single-cracked beams with 20% and 40% cracks further confirms the reliability of the index. Compared with the $\Delta(\Delta f)$ curves, the ζ curves exhibit reduced fluctuations and more clearly highlight the damage location through a prominent peak.

The main findings of this study can be summarized as follows:

1. The accuracy of the derived analytical expression for estimating the natural frequency of an Euler-Bernoulli beam carrying a mass with rotary inertia is verified across multiple types of boundary conditions. For the first ten natural frequencies, the error ranges from 0.05% to 3.24% for simply supported boundaries, 0.00% to 6.92% for clamped-free boundaries, 0.03% to 6.92% for clamped-clamped boundaries, 0.01% to 6.87% for clamped-pinned boundaries, and 0.01% to 8.08% for sliding-pinned boundaries.
2. The proposed crack location index ζ is 'baseline-free' because it relies on measured natural frequencies of the damaged beam and does not require modal tests on its intact state. Instead, it utilizes the theoretical modal properties of an equivalent intact beam, which are readily available in the literature [33].
3. The proposed index suppresses false peaks in the curve of $\Delta(\Delta f)$ and the best performance can be observed for the 2nd and 3rd modes where all false peaks except those near boundaries can be suppressed, allowing crack-induced peaks to be highlighted.

Fig. 25 Two other modes affecting 4th and 5th natural frequencies. (**a**) torsional mode shape, (**b**) bending mode shape (strong direction)

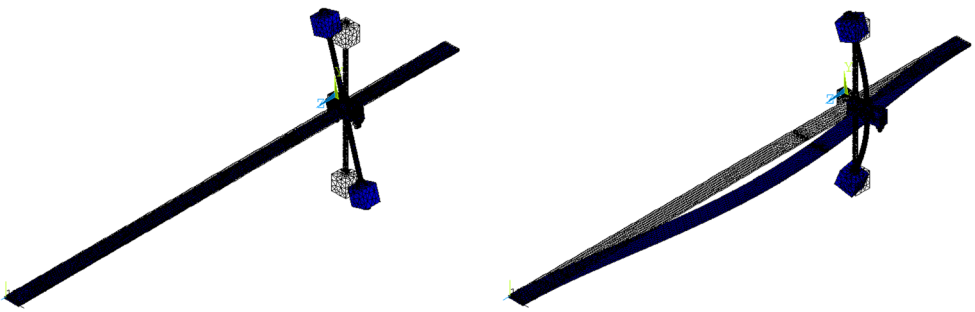

(a) torsional mode shape (b) bending mode shape (strong direction)

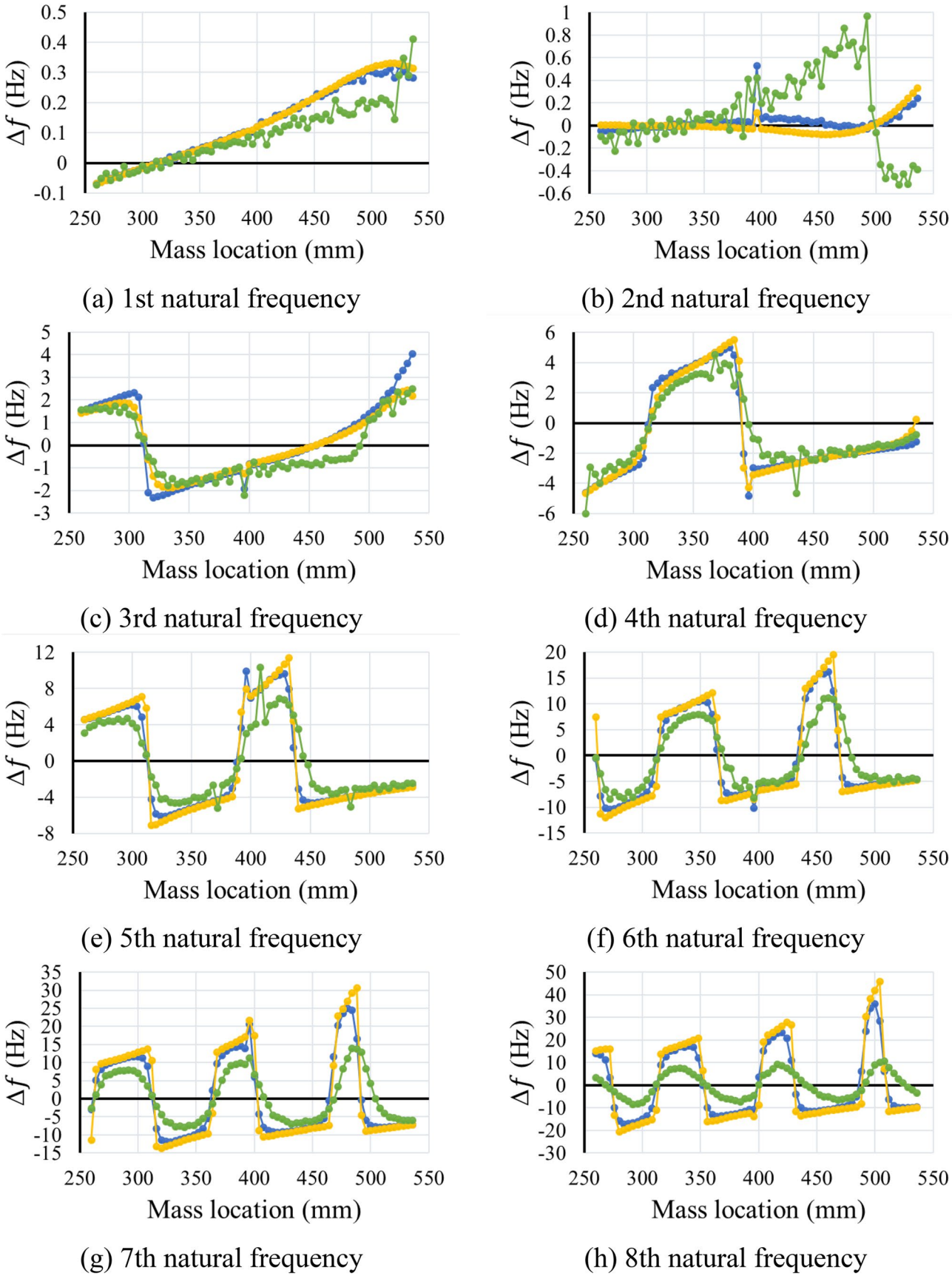
Δf (Hz)
Mass location (mm)
(a) 1st natural frequency
(b) 2nd natural frequency
(c) 3rd natural frequency
(d) 4th natural frequency
(e) 5th natural frequency
(f) 6th natural frequency
(g) 7th natural frequency
(h) 8th natural frequency
Experiment
ANSYS
DSM

Fig. 26 The comparison of natural frequency shift (Δf) results (20% crack at 394 mm). (**a**) 1 st natural frequency, (**b**) 2nd natural frequency, (**c**) 3rd natural frequency, (**d**) 4th natural frequency, (**e**) 5th natural frequency, (**f**) 6th natural frequency, (**g**) 7th natural frequency, (**h**) 8th natural frequency

4. Since the proposed index performs well with lower modes, using a larger roving rotary inertia is beneficial, whereas variations in the roving mass have a relatively weaker influence on the peak at the crack location.
5. The proposed index can be applied to different boundary conditions.
6. The proposed index can be used for detecting multiple cracks without missing identifications when the 2nd and 3rd modes are used jointly.
7. Using the proposed index, crack locations were identified accurately across all numerical studies. In the experimental validation, the crack location was pinpointed for the 40% cracked beam under all three rotary inertia settings; for the 20% cracked beam, the largest deviation between the true and identified crack locations was 8 mm, which is small compared with the length of the segment (i.e. 280 mm) being tested.

Based on these findings, some recommendations for future research are given as follows:

1. A limitation of the proposed index in its current form is its reduced reliability in regions near the beam's supports. This is because, for the boundary conditions considered, when the roving mass approaches boundaries, some of the displacement, slope, and curvature of all the bending modes approach zero, so the effect of the roving mass diminishes rapidly. This can change natural frequencies rapidly near supports, leading to false peaks in Δ (Δf) and ζ that obscure or mimic the signature of a crack. Since damage often occurs near supports in real-world structures, addressing this limitation is a critical next step. One promising approach is to leverage advanced signal processing such as in [14] where the wavelet feature extraction-based damage detection index demonstrates satisfactory accuracy when detecting damage in the end regions of concrete-filled steel tubes.
2. Numerical results indicate that the proposed index for the 1 st mode can also support crack identification. The measurability check in Appendix B also confirms that the crack-induced frequency shift is measurable for the 1 st mode. In the experiment, however, the frequency shift in the 1 st mode was largely obscured by measurement noise when plotted together with results from other mass locations. Integrating the index with signal processing approaches, for example wavelet-based methods [43], may help improve detection capability when noise is present.
3. Future work could investigate how to generalize the proposed index to beams with more complex boundary conditions, where the modal characteristics of the corresponding intact beam may not be directly accessible. One possibility is to examine whether the intact beam's modal properties could be inferred in an inverse manner using Eq. (20).
4. The proposed index has been shown to identify multiple cracks, but situations involving closely spaced cracks or distributed damage warrant further investigation. In such cases, the distinct crack-induced peaks revealed by the index may merge and become less distinguishable. Advanced signal processing such as wavelet transform may help isolate and sharpen these local perturbations.
5. A useful extension would be to benchmark the proposed index against existing damage indicators, such as those based on modal curvature [44] or modal strain energy [45].

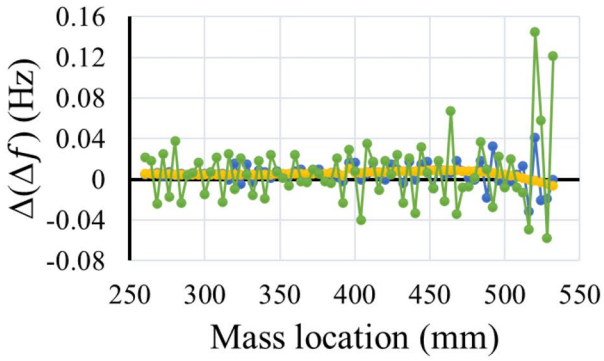

(a) 1st natural frequency

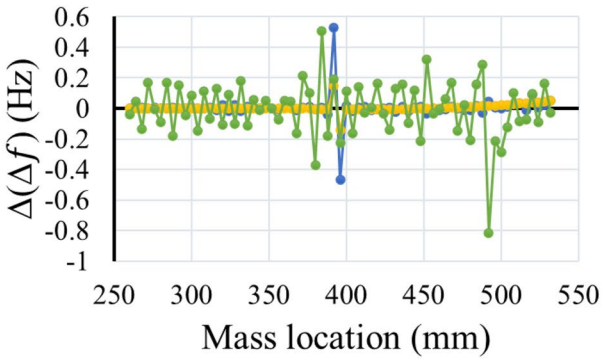

(b) 2nd natural frequency

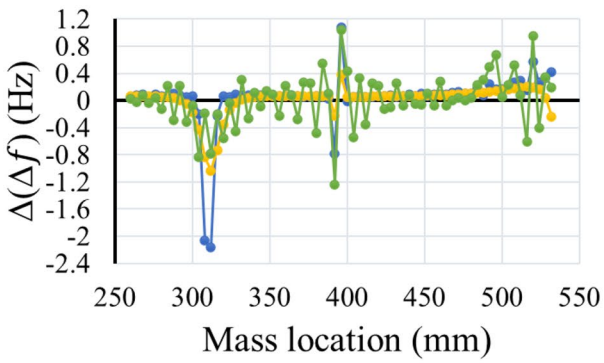

(c) 3rd natural frequency

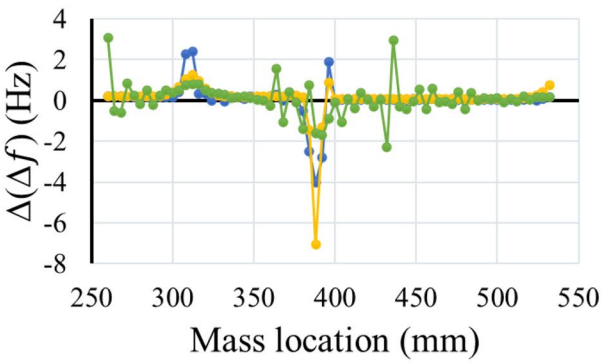

(d) 4th natural frequency

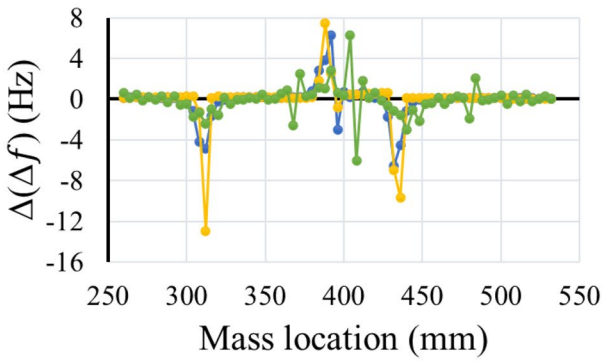

(e) 5th natural frequency

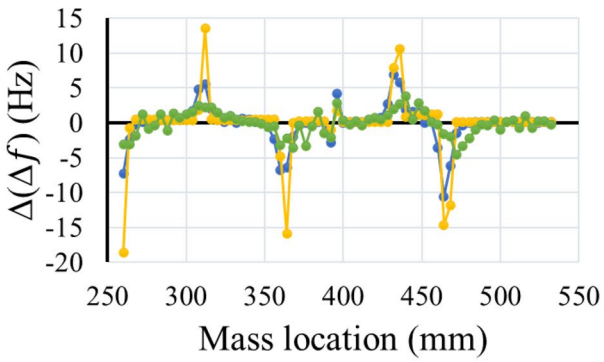

(f) 6th natural frequency

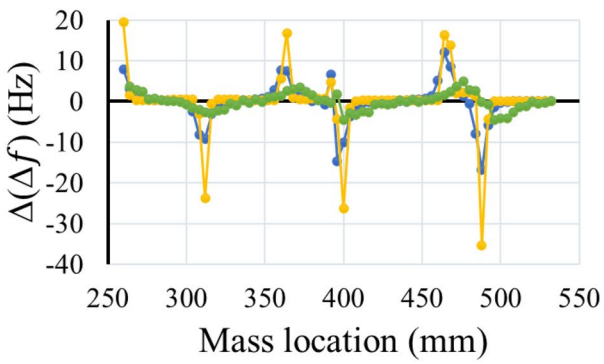

(g) 7th natural frequency

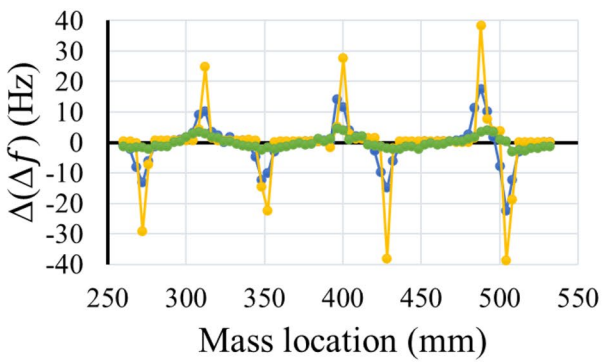

(h) 8th natural frequency

Experiment ANSYS DSM

Fig. 27 The comparison of the change of natural frequency shift ($\Delta(\Delta f)$) results (20% crack at 394 mm). (**a**) 1 st natural frequency, (**b**) 2nd natural frequency, (**c**) 3rd natural frequency, (**d**) 4th natural frequency, (**e**) 5th natural frequency, (**f**) 6th natural frequency, (**g**) 7th natural frequency, (**h**) 8th natural frequency

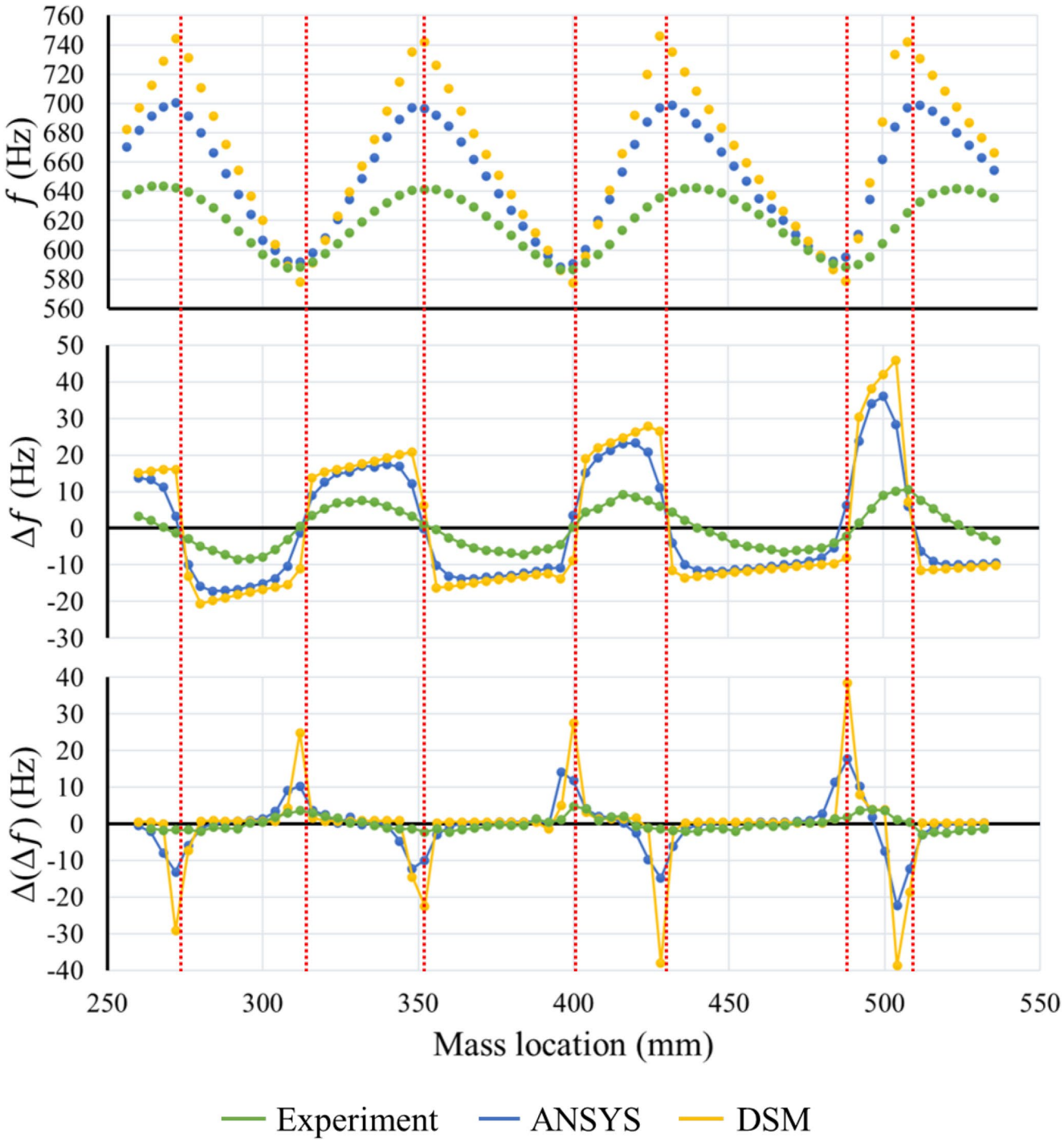

Fig. 28 The comparison of f, Δf, and $\Delta(\Delta f)$ for the 8th natural frequency (20% crack at 394 mm. The red dotted lines indicate the mass locations corresponding to the extrema of the curve of natural frequency)

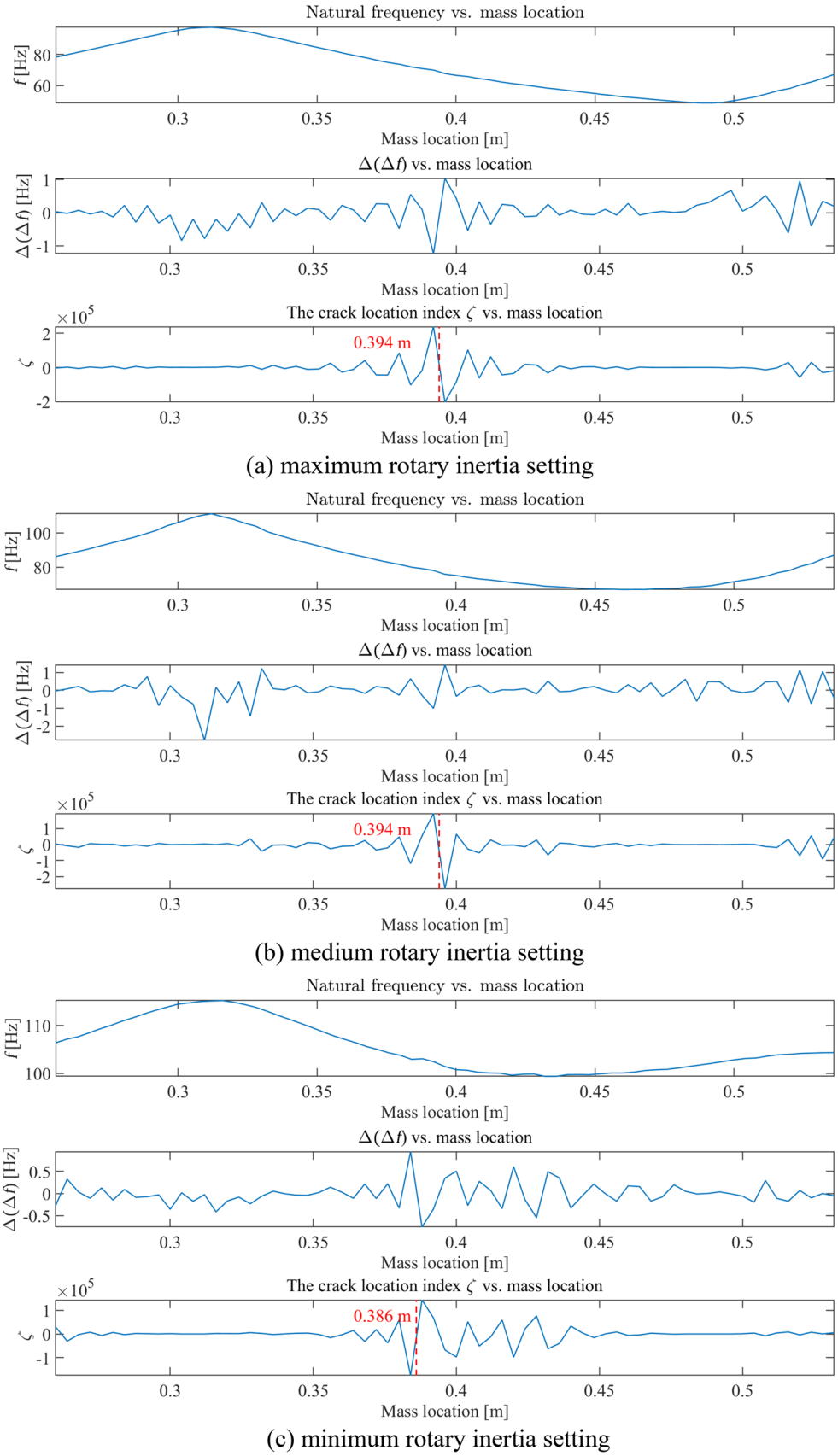

Fig. 29 The natural frequency data and ζ of the 3rd mode of the 20% cracked beam carrying a roving mass with rotary inertia (crack location: 0.394 m). (**a**) maximum rotary inertia setting, (**b**) medium rotary inertia setting, (**c**) minimum rotary inertia setting

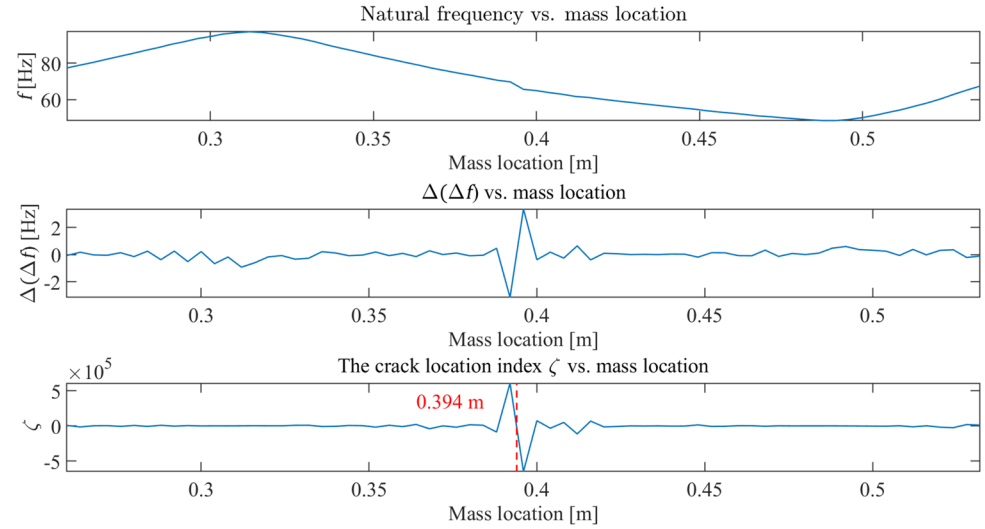

(a) maximum rotary inertia setting

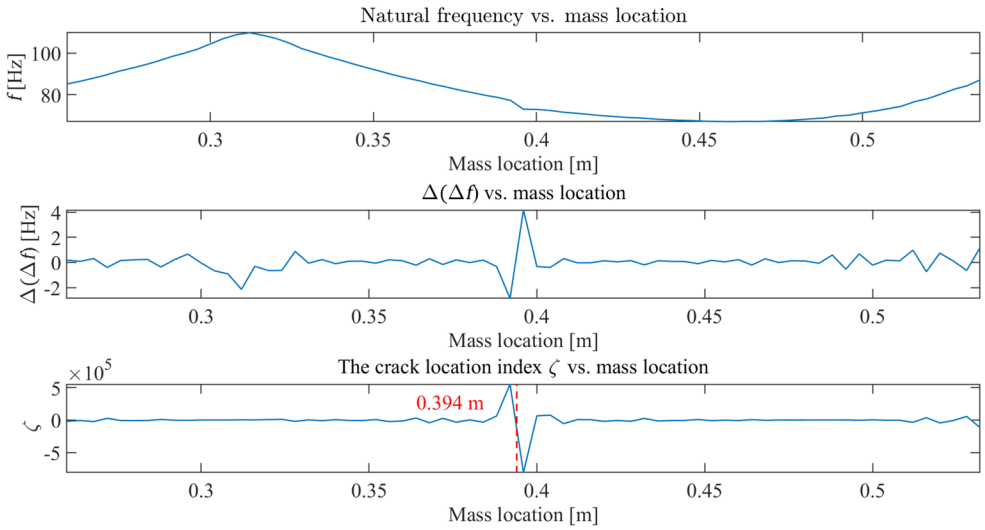

(b) medium rotary inertia setting

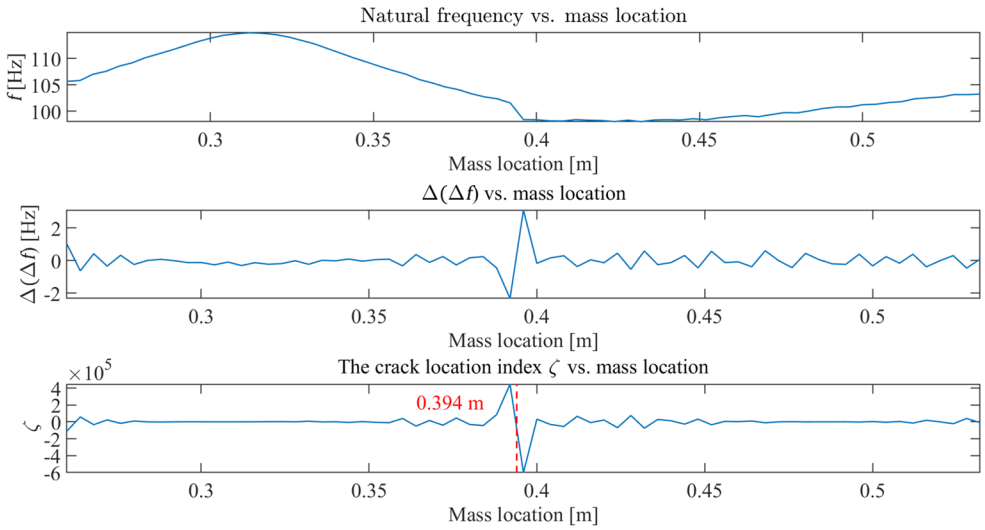

(c) minimum rotary inertia setting

Fig. 30 The natural frequency data and ζ of the 3rd mode of the 40% cracked beam carrying a roving mass with rotary inertia (crack location: 0.394 m). (**a**) maximum rotary inertia setting, (**b**) medium rotary inertia setting, (**c**) minimum rotary inertia setting

Appendix A. Verification of the Natural Frequency Estimation Equation across Multiple Boundary Conditions

To further validate the accuracy of Eq. (20), natural frequencies are calculated for the beam in Fig. 3 with different boundary conditions. The results are compared with the DSM results and presented below.

Table 3 Natural frequencies obtained through the DSM and Eq. (20) forclamped-free boundary conditions

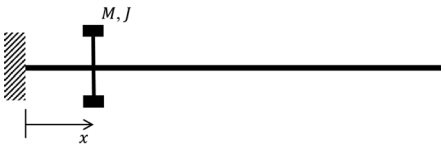

Mode number	DSM results (rad/s)	Eq. (20) results (rad/s)	Percentage error (%)
1	71.12	71.12	0.00
2	441.01	441.12	0.03
3	1186.72	1190.31	0.30
4	2243.80	2238.48	0.24
5	3732.07	3650.13	2.20
6	5711.78	5553.04	2.78
7	8067.03	8025.97	0.51
8	10612.90	11219.44	5.72
9	13497.17	14431.21	6.92
10	17024.35	18026.19	5.88

Table 4 Natural frequencies obtained through the DSM and Eq. (20) forclamped-clamped boundary conditions

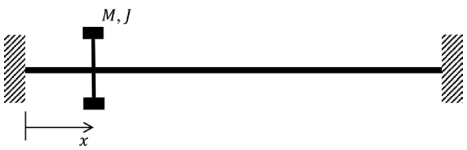

Mode number	DSM results (rad/s)	Eq. (20) results (rad/s)	Percentage error (%)
1	447.52	447.65	0.03
2	1186.46	1190.01	0.30
3	2243.76	2238.46	0.24
4	3732.08	3650.13	2.20
5	5711.78	5565.94	2.55
6	8067.03	8025.97	0.51
7	10612.90	11219.44	5.72
8	13497.17	14431.21	6.92
9	17024.35	18026.19	5.88
10	20708.91	22020.92	6.34

Table 5 Natural frequencies obtained through the DSM and Eq. (20) forclamped-pinned boundary conditions

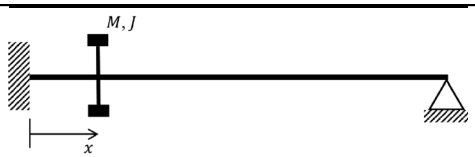

Mode number	DSM results (rad/s)	Eq. (20) results (rad/s)	Percentage error (%)
1	310.11	310.14	0.01
2	972.57	974.69	0.22
3	1945.14	1947.00	0.10
4	3313.01	3255.44	1.74
5	5174.50	5033.58	2.72
6	7454.56	7353.04	1.36
7	9960.06	10484.98	5.27
8	12720.88	13594.65	6.87
9	16085.15	17089.93	6.25
10	19886.97	20984.79	5.52

Table 6 Natural frequencies obtained through the DSM and Eq. (20) for sliding-pinned boundary conditions

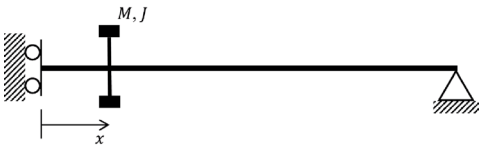

Mode number	DSM results (rad/s)	Eq. (20) results (rad/s)	Percentage error (%)
1	45.84	45.84	0.01
2	431.19	428.48	0.63
3	1236.20	1240.06	0.31
4	2408.70	2430.48	0.90
5	3845.30	3855.26	0.26
6	5649.54	5542.30	1.90
7	7958.77	7738.50	2.77
8	10614.74	10703.30	0.83
9	13369.67	14332.98	7.21
10	16564.25	17903.13	8.08

Table 7 Natural frequencies obtained through the DSM and Eq. (20) for sliding-pinned boundary conditions

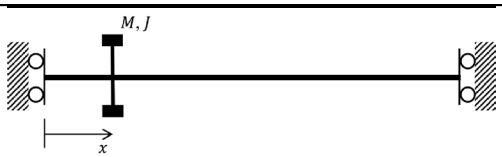

Mode number	DSM results (rad/s)	Eq. (20) results (rad/s)	Percentage error (%)
1	187.30	186.22	0.57
2	781.66	777.86	0.49
3	1784.25	1784.46	0.01
4	3094.66	3089.85	0.16
5	4686.94	4635.69	1.09
6	6744.15	6564.00	2.67
7	9263.24	9047.55	2.33
8	11978.00	12030.78	0.44
9	14871.14	15197.56	2.20
10	18474.65	18438.81	0.19

Appendix B. Measurability Check of the 20% Cracked Beam

Suppose κ is the magnitude of error in experimental frequency results (caused by uncertainties in measurement, inaccuracies in mass placement, human factors, etc.) and f_{true} is the true value of natural frequency, the experimental frequency results can be expressed as

$$f = f_{true} \pm \kappa \tag{B1}$$

According to Eqs. (24)-(25), natural frequency shift can be written as

$$\bigtriangleup f = \bigtriangleup f_{true} \pm 2\kappa \tag{B2}$$

and the change of natural frequency shift can be written as

$$\bigtriangleup\left(\bigtriangleup f\right) = \bigtriangleup\left(\bigtriangleup f_{true}\right) \pm 4\kappa \tag{B3}$$

The measurability of Δf and $\Delta\ (\Delta f)$ when the mass passes the crack can be confirmed if $|\Delta f| > 2\kappa$ and $|\Delta\ (\Delta f)| > 4\kappa$.

To estimate the values of κ, repeatability checks are required. In the experiment, the bolts securing the roving mass were manually tightened to approximate a rigid connection between the mass and the beam. After each impact hammer test, the bolts were loosened so the mass could be moved to the next location, then retightened before the subsequent test. Throughout this procedure, variations in bolt-tightening torque and small inaccuracies in mass positioning could introduce additional variability into the measured natural frequencies. Therefore, it is necessary to examine the repeatability of the measured natural frequencies by repeatedly loosening and retightening the bolts. With an acceptable repeatability check, the variance caused by bolt-tightening torque and small error in mass positioning can be considered negligible, allowing the observed frequency shifts to be attributed solely to the presence of the crack and the roving mass.

Fig. 31 shows the magnitude plot of FRF of five repeatability tests conducted on an intact beam carrying the roving mass with the maximum rotary inertia setting. The roving mass was positioned 0.36m from the beam's left end. Between successive tests, the mass was removed and then reattached at the same location. The five curves show virtually minor difference from one another, indicating that the test setup achieved high repeatability.

Table 8 presents the first eight natural frequencies obtained from the repeatability tests, along with the corresponding standard deviations. The variations across tests are very small, further confirming the high repeatability of the measurements.

The values of can be estimated using the standard deviation between the repeatability tests in Table 8. When the mass passed the 20% crack, the measured using different rotary inertia settings is compared with in Table 9, and the comparison between and is made in Table 10. From the comparison, and are generally larger than and, respectively. Thus the measurability of frequency changes when the roving mass passed the 20% crack in the experiment can be confirmed.

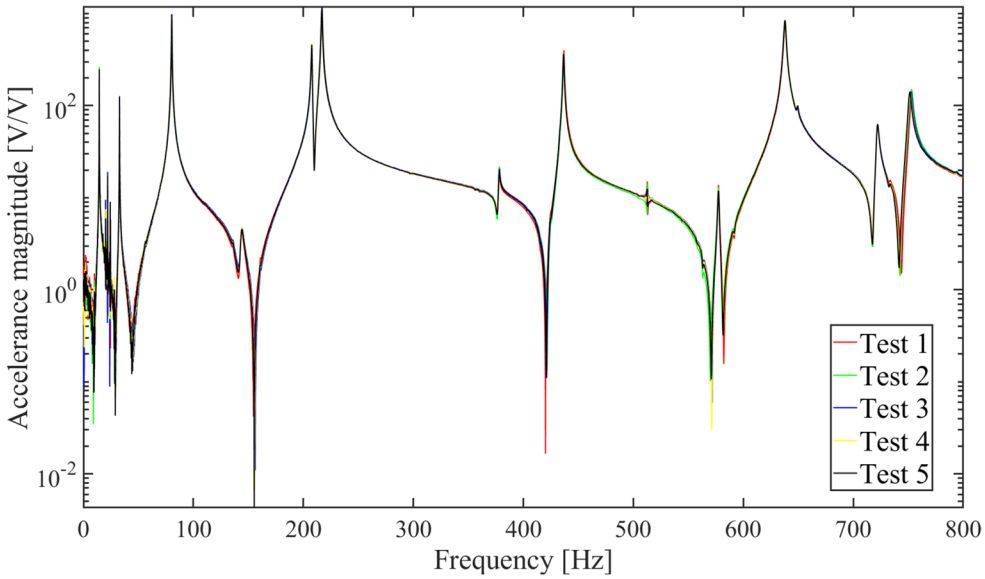

Fig. 31 The accelerance FRF magnitude of five repeatability tests

Table 8 The natural frequency results of five repeatability tests

Mode number	Natural frequency results (Hz)					Standard deviation
	Test 1	Test 2	Test 3	Test 4	Test 5	
1	14.3954	14.3963	14.3924	14.3918	14.3902	0.0026
2	32.8590	32.8759	32.8832	32.8575	32.8295	0.0208
3	80.4844	80.4221	80.3685	80.3327	80.2926	0.0753
4	144.4534	144.0717	144.0472	143.5125	143.4537	0.4203
5	217.0632	216.9812	216.8912	216.8645	216.8626	0.0876
6	377.9789	378.2351	378.1126	378.0502	377.8934	0.1301
7	436.8046	436.7572	436.7101	436.5743	436.6282	0.0937
8	638.1071	638.0135	638.0793	638.0734	637.9210	0.0742

Table 9 The comparison between Δf and 2κ (unit: Hz)

Mode number	2κ	Δf with different rotary inertia settings		
		Maximum	Medium	Minimum
1	0.0051	0.0622	0.1011	0.1096
2	0.0415	0.4220	0.4529	−0.2303
3	0.1506	−2.2019	−2.1366	−0.9875
4	0.8405	−0.1157	−1.2055	−5.3741
5	0.1751	3.0519	5.0702	10.3636
6	0.2602	−8.2519	−9.6268	−10.6534
7	0.1875	11.2656	15.5167	20.6261
8	0.1484	−4.4400	−8.0386	−11.8222

Table 10 The comparison between $\Delta\ (\Delta f)$ and 4κ (unit: Hz)

Mode number	4κ	$\Delta\ (\Delta f)$ with different rotary inertia settings		
		Maximum	Medium	Minimum
1	0.0102	−0.0231	0.0202	0.0147
2	0.0830	0.1910	0.4617	0.2268
3	0.3012	−1.2334	−1.0042	−0.3507
4	1.6810	−1.7065	−2.1394	−4.4697
5	0.3503	2.8014	4.7191	8.7810
6	0.5203	−2.1050	−3.3794	−4.6859
7	0.3749	1.8027	5.6699	9.9282
8	0.2968	1.2157	0.4961	−2.6686

Acknowledgements None.

Funding Open Access funding enabled and organized by CAUL and its Member Institutions

Declarations

Competing Interests The authors have no competing interests to declare that are relevant to the content of this article.The authors have no competing interests to declare that are relevant to the content of this article.

References

1. Gomes GF, Mendez YAD, da Silva Lopes Alexandrino P, da Cunha SS, Ancelotti AC (2019) A review of vibration based inverse methods for damage detection and identification in mechanical structures using optimization algorithms and ann. Arch Comput Methods Eng 26(4):883–897. https://doi.org/10.1007/s11831-018-9273-4
2. Sun X, Ilanko S, Mochida Y, Tighe RC (2023) A review on vibration-based damage detection methods for civil structures. Vibration 6(4):843–875. https://doi.org/10.3390/vibration6040051
3. Khanahmadi M, Mirzaei B, Dezhkam B, Rezaifar O, Gholhaki M, Amiri GG (2024) Vibration-based health monitoring and damage detection in beam-like structures with innovative approaches based on signal processing: A numerical and experimental study. Structures 68:107211. https://doi.org/10.1016/j.istruc.2024.107211
4. Zhu J, Zhang Y (2023) Damage detection for bridge structures under vehicle loads based on frequency decay induced by breathing cracks. Struct Infrastruct Eng 19(6):793–809. https://doi.org/10.1080/15732479.2021.1979601
5. Nick H, Ashrafpoor A, Aziminejad A (2023) Damage identification in steel frames using dual-criteria vibration-based damage detection method and artificial neural network. Structures 51:1833–1851. https://doi.org/10.1016/j.istruc.2023.03.152
6. Brethee KF, Uwayed AN, Alden Qwam AY (2023) A novel index for vibration-based damage detection technique in laminated composite plates under forced vibrations: experimental study. Struct Health Monit 22(5):3109–3125. https://doi.org/10.1177/14759217221145622
7. He M, Yang T, Du Y (2017) Nondestructive identification of composite beams damage based on the curvature mode difference. Compos Struct 176:178–186. https://doi.org/10.1016/j.compstruct.2017.05.040
8. Namah AI, Brethee KF (2025) Free vibration characteristics and localization of single and multiple cracks within beam structure. World J Eng. https://doi.org/10.1108/WJE-04-2025-0212.ahead-of-print(ahead-of-print)
9. Betti M, Facchini L, Biagini P (2015) Damage detection on a three-storey steel frame using artificial neural networks and genetic algorithms. Meccanica 50(3):875–886. https://doi.org/10.1007/s11012-014-0085-9
10. Avci O, Abdeljaber O, Kiranyaz S, Hussein M, Gabbouj M, Inman DJ (2021) A review of vibration-based damage detection in civil structures: from traditional methods to machine learning and deep learning applications. Mech Syst Signal Process 147:107077. https://doi.org/10.1016/j.ymssp.2020.107077
11. Hakim SJS, Abdul Razak H, Ravanfar SA (2015) Fault diagnosis on beam-like structures from modal parameters using artificial neural networks. Measurement 76:45–61. https://doi.org/10.1016/j.measurement.2015.08.021
12. Khanahmadi M, Gholhaki M, Rezaifar O, Dezhkam B (2023) Signal processing methodology for detection and localization of damages in columns under the effect of axial load. Measurement 211:112595. https://doi.org/10.1016/j.measurement.2023.112595
13. Khanahmadi M, Mirzaei B, Amiri GG, Gholhaki M, Rezaifar O (2024) Vibration-based damage localization in 3d sandwich panels using an irregularity detection index (idi) based on signal processing. Measurement 224:113902. https://doi.org/10.1016/j.measurement.2023.113902
14. Khanahmadi M, Mirzaei B, Amiri GG, Gholhaki M, Rezaifar O (2025) A mode shape sensitivity-based wavelet feature extraction method for interface debonding detection in concrete-filled steel tubes. Meas Sci Technol 36(1):016137. https://doi.org/10.1088/1361-6501/ad8adf
15. Khanahmadi M, Mirzaei B, Amiri GG, Gholhaki M, Rezaifar O (2024) A numerical study on vibration-based interface debonding detection of Cfst columns using an effective wavelet-based feature extraction technique. Steel Compos Struct 53(1):45–59. https://doi.org/10.12989/scs.2024.53.1.045
16. Sun X, Ilanko S, Mochida Y, Tighe RC (2024) A study on the feasibility of natural frequency-based crack detection. Appl Sci 14(24):11712. https://doi.org/10.3390/app142411712
17. Zhong S, Oyadiji SO (2008) Identification of cracks in beams with auxiliary mass Spatial probing by stationary wavelet transform. J Vib Acoust 130(4):041001. https://doi.org/10.1115/1.2891242
18. Yang C, Oyadiji SO (2017) Damage detection using modal frequency curve and squared residual wavelet coefficients-based damage indicator. Mech Syst Signal Process 83:385–405. https://doi.org/10.1016/j.ymssp.2016.06.021
19. Zhang Y, Wang L, Lie ST, Xiang Z (2013) Damage detection in plates structures based on frequency shift surface curvature. J Sound Vib 332(25):6665–6684. https://doi.org/10.1016/j.jsv.2013.07.028
20. Zhang Y, Lie ST, Xiang Z, Lu Q (2014) A frequency shift curve based damage detection method for cylindrical shell structures. J Sound Vib 333(6):1671–1683. https://doi.org/10.1016/j.jsv.2013.11.026
21. Zhong S, Zhong J, Zhang Q, Maia N (2017) Quasi-optical coherence vibration tomography technique for damage detection in beam-like structures based on auxiliary mass induced frequency shift. Mech Syst Signal Process 93:241–254. https://doi.org/10.1016/j.ymssp.2017.02.005
22. Wang L, Lie ST, Zhang Y (2016) Damage detection using frequency shift path. Mech Syst Signal Process 66:298–313. https://doi.org/10.1016/j.ymssp.2015.06.028
23. Fang S-E, Perera R (2009) Power mode shapes for early damage detection in linear structures. J Sound Vib 324(1):40–56. https://doi.org/10.1016/j.jsv.2009.02.002
24. Solís M, Ma Q, Galvín P (2018) Damage detection in beams from modal and wavelet analysis using a stationary roving mass and

noise Estimation. Strain 54(2):e12266. https://doi.org/10.1111/str.12266
25. Lie S, Zhang Y, Wang L (2015) Damage detection in compressed natural gas (cng) cylinders based on auxiliary mass induced frequency shift. Exp Mech 55(3):487–498. https://doi.org/10.1007/s11340-014-9960-5
26. Wang L, Zhang Y, Lie ST (2017) Detection of damaged supports under railway track based on frequency shift. J Sound Vib 392:142–153. https://doi.org/10.1016/j.jsv.2016.11.018
27. Nguyen KV (2016) Crack detection of a double-beam carrying a concentrated mass. Mech Res Commun 75:20–28. https://doi.org/10.1016/j.mechrescom.2016.05.009
28. Haji ZN, Olutunde Oyadiji S (2014) The use of roving discs and orthogonal natural frequencies for crack identification and location in rotors. J Sound Vib 333(23):6237–6257. https://doi.org/10.1016/j.jsv.2014.05.046
29. Cannizzaro F, De Los Rios J, Caddemi S, Caliò I, Ilanko S (2018) On the use of a roving body with rotary inertia to locate cracks in beams. J Sound Vib 425:275–300. https://doi.org/10.1016/j.jsv.2018.03.020
30. Sun X (2021) The application of the wittrick-williams algorithm for free vibration analysis of cracked skeletal structures. Thin-Walled Struct 159:107307. https://doi.org/10.1016/j.tws.2020.107307
31. Ilanko S, Mochida Y, De Los Rois J (2018) Vibration analysis of cracked structures as a roving body passes a crack using the rayleigh-ritz method. EPI International Journal of Engineering 1(2):30–34. https://doi.org/10.25042/epi-ije.082018.04
32. Sun X, Ilanko S, Mochida Y, Tighe RC, Mace BR (2025) Theoretical and experimental investigation of the use of a roving mass with rotary inertia for crack detection in beam-like structures. J Vib Eng Technol 13(1):105. https://doi.org/10.1007/s42417-024-01735-z
33. Blevins RD, Plunkett R (1979) Formulas for natural frequency and mode shape. Van Nostrand Reinhold Co., New York
34. Banerjee JR, Guo S On the dynamics of cracked beams. in 50th AIAA/ASME/ASCE/AHS/ASC Structures, Structural Dynamics, and, Conference M (2009) California, USA: American Institute of Aeronautics and Astronautics
35. Su H, Banerjee JR (2013) Free vibration of a cracked timoshenko beam using the dynamic stiffness method. in 11th International Conference on Vibration Problems. Lisbon, Portugal: Nova University of Lisbon
36. Wan C, Jiang H, Xie L, Yang C, Ding Y, Tang H, Xue S (2020) Natural frequency characteristics of the beam with different cross sections considering the shear deformation induced rotary inertia. Appl Sci 10(15):5245. https://doi.org/10.3390/app10155245
37. Rao SS (2017) Mechanical vibrations. Pearson Education
38. Chiarelli MR (2025) Dynamic response of beams under random loads. Mathematics 13(8):1322. https://doi.org/10.3390/math13081322
39. Qian C, Chen C, Zhou G, Dai L (2012) Dynamic response analysis for elastic bearing beam under moving load. Nonlinear Eng 1(3–4):109–114. https://doi.org/10.1515/nleng-2012-0007
40. Michaltsos GT (2002) Dynamic behaviour of a single-span beam subjected to loads moving with variable speeds. J Sound Vib 258(2):359–372. https://doi.org/10.1006/jsvi.2002.5141
41. Biggs JM (1964) Introduction to structural dynamics. McGraw-Hill Professional
42. Ewins DJ (2009) Modal testing: Theory, practice and application. Wiley
43. Li D, Xu Z, Ostachowicz W, Cao M, Liu J (2020) Identification of multiple cracks in noisy conditions using scale-correlation-based multiscale product of swpt with laser vibration measurement. Mech Syst Signal Process 145:106889. https://doi.org/10.1016/j.ymssp.2020.106889
44. Altunışık AC, Okur FY, Karaca S, Kahya V (2019) Vibration-based damage detection in beam structures with multiple cracks: modal curvature vs. modal flexibility methods. Nondestr Test Eval 34(1):33–53. https://doi.org/10.1080/10589759.2018.1518445
45. Wang S, Xu M (2019) Modal strain energy-based structural damage identification: a review and comparative study. Struct Eng Int 29(2):234–248. https://doi.org/10.1080/10168664.2018.1507607